ORBIT AND FORMATION CONTROL FOR LOW-EARTH-ORBIT GRAVIMETRY DRAG-FREE SATELLITES

ORBIT AND FORMATION CONTROL FOR LOW-EARTH-ORBIT GRAVIMETRY DRAG-FREE SATELLITES

Enrico Canuto,[*] Luigi Colangelo,[†] Marcello Buonocore[‡], Luca Massotti[**] and Bénédicte Girouart[***]

The paper outlines orbit and formation control of a long-distance (>100 km) two-satellite formation for the Earth gravity monitoring. Orbit control applies to a single satellite and performs altitude control. Here formation control is formulated as a control capable of altitude and distance control at the same time. The satellites being placed in a low Earth orbit, orbit and formation control employ the measurements of a global navigation system. Formation control is imposed by long-distance laser interferometry, which is the key instrument for gravity measurement. Orbit and formation control are low-frequency control systems in charge of cancelling bias and drift of the residual drag-free accelerations. Drag-free control is the core of the orbit/formation control since it allows the formation to fly drag-free only subject to gravity. Drag-free control being required to have a bandwidth close to 1 Hz, is designed as the inner loop of the formation control. In turn, formation control must not destroy drag-free performance, which objective demands that formation control be effective only below the 0.2 mHz orbital frequency. Control design is based on a new orbit and formation dynamics, which are compared with the classical Hill-Clohessy-Wiltshire equations. The new dynamic equations are the first step in building the embedded model, which is the core of the control unit. Embedded model derivation is explained only for the orbit control, and briefly mentioned for the formation control. Simulated results are provided. Drag free results are compared with GOCE experimental data.

Keywords: orbit control, formation control, drag-free control, satellite, gravimetry

[*] Dipartimento di Automatica e Informatica, Politecnico di Torino, Corso Duca degli Abruzzi 24, 10129 Torino, Italy, phone +390110907026, enrico.canuto@polito.it, contact author

[†] Dipartimento di Automatica e Informatica, Politecnico di Torino, Corso Duca degli Abruzzi 24, 10129 Torino, Italy, luigi.colangelo@polito.it

[‡‡] Thales Alenia Space Italia, Strada Antica di Collegno, 253, 10146 Torino, marcello.buonocore@thalesaleniaspace.com

** ESA-ESTEC, EOP-SFP, Keplerlaan 1, 2200 AG Noordwijk ZH, The Netherlands, luca.massotti@esa.int

*** ESA-ESTEC, TEC-ECC, Keplerlaan 1, 2200 AG Noordwijk ZH, The Netherlands, benedicte.girouart@esa.int

INTRODUCTION

Drag-free concepts

Post ESA's GOCE (Gravity field and steady state Ocean Circulation Explorer [1], [2], [3]) and post GRACE (GRAvity recovery and Climate Experiment, [4]) space Earth gravimetry missions, gravitational wave observatories like LISA (Laser Interferometer Space Antenna [5]), equivalence principle experiments like MICROSCOPE (MICRO-Satellite a traînee Compensée pour l'Observation du Principe d'Equivalence, [6]) will rely on a formation of free falling 'proof masses' and on the measurement of their distance variations for revealing anomalies and variations of the local gravity field. A spacecraft hosting in a proper cage free falling masses is referred to as drag-free satellites, since drag must be cancelled to keep proof masses free in the cage. Two alternatives are possible.

1) *Free-falling mass concept*. The satellite chases and centers in the cage the proof mass through a control system, which is fed by proof-mass position sensors and is actuated by thrusters mounted on the cage. The gravitational mass motion becomes very clean except for parasitic forces to be abated by construction. The satellite becomes drag-free by tracking the proof mass and not by directly rejecting non-gravitational forces. Only a single proof mass can be tracked: two or more free-falling masses may be arranged as the shells of the inner proof mass as in the MICROSCOPE payload [6]. As an alternative, other proof-masses may be actively suspended to the cage as in the accelerometer concept. LISA Pathfinder [7] has been adopted an assembly of this kind.

2) *Accelerometer concept*. The proof mass is arranged with an active suspension system that keeps the mass centered in the cage and performs initial centering after launch. As the suspension force provides a measurement of the non-gravitational forces acting on the satellite, they can be directly cancelled by thrusters commanded by a drag-free control. The paper is concerned with this solution. Many accelerometers can be mounted on a single satellite like on GOCE, where three orthogonal pairs of proof masses 0.5 m distant constituted a 3D gradiometer.

In principle, both solutions can coexist like in LISA [5] and Gravity Probe B [8], since active suspensions may be employed for mass centering, and subsequently switched off.

Future missions technology and requirements

Performance of gravimetry by means of a long-distance formation as in GRACE (>100 km distance), but at lower altitude (300 to 400 km), may be improved by making each satellite drag-free and by disposing of an accurate distance measurement like that provided by laser interferometers. Satellite-to satellite distance variations must be measured along the satellite-to–satellite line (SSL) which is defined as the line connecting the satellites centres-of-mass (CoM) C_1 and C_2 (see Figure 3). In a low-Earth-orbit, the SSL can be materialized by differential global navigation system instruments (GNSI). GNSI materialization is necessary for formation control, whereas laser beam materialization is employed by attitude control [9].

A first set of requirements comes from the scientific data elaboration and specifically from the calibration of the GOCE-class accelerometers. The main requirements concern non-gravitational CoM accelerations and angular accelerations as they must be ideally brought to zero, actually below the spectral bounds in Table 1.

A second set of requirements concerns formation control. Requirements have been split into distance, radial and lateral variations with respect to a nominal circular orbit. Lateral variation refers to in-line formation, where two satellites stay on the same nominal orbit. In the case of pendulum formation (see Figure 3) the two satellites move on crossing orbits and the requirement is expressed in terms of the cone swept by the SSL during a single orbit. Formation requirements appear at first sight rather loose being expressed as a percentage of the nominal distance (> 100

km). Actually, formation control must guarantee formation stability, i.e. that the perturbations of a nominal formation remain bounded during the whole mission life (> 10 years).

Table 1. Drag-free and formation control requirements

No	Variable	Unit	Bound	Frequency range, bound type
Drag free control				
1	3D CoM acceleration	$\mu m/s^2/\sqrt{Hz}$	0.01	> 1mHz, PSD
2	idem	$\mu m/s^2$	1	whole, max
3	3D angular acceleration	$\mu rad/s^2/\sqrt{Hz}$	0.01	> 1mHz, PSD
4	idem	$\mu rad/s^2$	1	whole, max
Formation control				
5	Formation distance variation	% (distance)	5	whole, max
6	Formation radial variation	% (distance)	2	whole, max
7	Mean orbit height variation	m	50	< 0.2 mHz, max
8	Formation lateral variation	% (distance)	1	whole, max (in line formation)
9	Max formation semi-aperture	rad	0.18	whole, max (pendulum formation)

Formation control requires knowing the relative satellite position, which is provided by differential GNSI like GPS receivers. Drag-free control requires one or more accelerometers capable of providing linear and angular accelerations. Drag-free, formation and attitude control are actuated by a propulsion assembly (all-propulsion satellite as in [13] and [14]), consisting of eight small proportional thrusters capable of a few millinewton thrust.

Control architecture and design

The design of the Orbit and Attitude Control System (AOCS) is tackled with the aid of the Embedded Model Control (EMC, [15], [16]), which calls for a hierarchical and multi-rate control unit around the real-time embedded model of the satellite controllable dynamics. The latter is complemented by the 'stochastic dynamics' of the disturbance to be rejected. The ensemble of the two dynamics must be observable by the available measurements.

Formation and center-of-mass (CoM) drag-free control (also referred to as linear drag-free) may be considered as subsystems of the orbit control. Here however, formation control is defined and designed to encompass orbit control, which latter is restricted to altitude control. Formation control is designed to perform altitude control of both satellites together with distance and angular control, which implies that orbit control is a whole with formation control. To the purpose, a new set of orbit and formation perturbation equations has been developed. Formation angular control can be fully decoupled from distance/altitude control and will not be treated here.

Drag-free control, being wide band, plays the role of an inner loop, thus approaching an ideal, zero-disturbance actuator only affected by accelerometer bias and drift. In addition, attitude control takes advantage of a wide-band angular drag-free control (inner loop), which is demanded to zero

angular accelerations for similar reasons to linear drag-free control. Alternative design of drag-free satellites has been made in the frequency domain as in [17], [18] and [19].

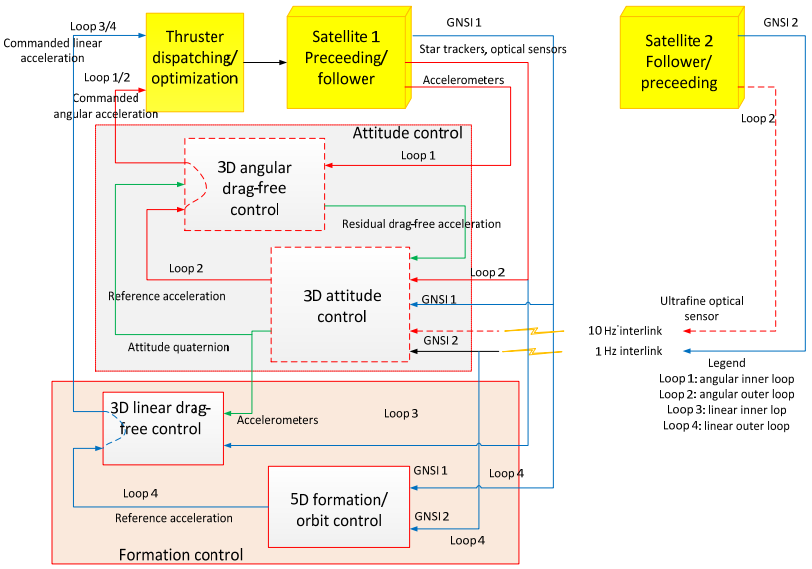

Figure 1 Higher-level block-diagram of the AOCS architecture.

To provide a better insight of the inner- and outer-loop architecture, the higher-level block-diagram of the science-phase AOCS is shown in Figure 1. Loops 1 and 2 in Figure 1 pertain to attitude control [9]. Loops 3 and 4 pertain to the orbit/formation control that exploits the wide band (>5 Hz) of the linear acceleration measurements in order to zero non-gravitational forces, leaving intact gravity accelerations, as they are the science objective. Zero acceleration can only be achieved in a limited frequency band (see Figure 2, above 1 mHz) so as to allow actuation of the formation control in a lower frequency band. The control algorithm which is referred to as 'linear drag-free' plays the role of an inner loop. It provides the outer loop with a wide-band, noise-free actuation channel. The outer loop is in charge of stabilizing the mean satellite formation geometry, leaving intact formation fluctuations due to gravity. The outer loop must be frequency-coordinated with the inner loop, which corresponds to say that orbit commands become the smooth reference of the drag-free control.

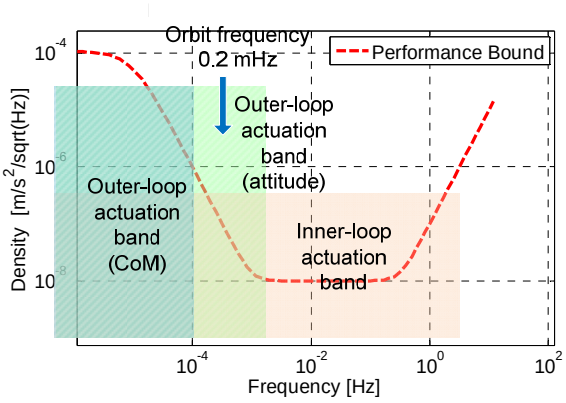

Figure 2 Frequency coordination of inner and outer loops.

The only coupling between orbit and attitude occurs in the conversion of the orbit commands from orbital to body frame, which is obtained through attitude quaternion. Because orbital and body frames must be accurately aligned by attitude control, better than one milliradian, since the early

mission phases, explicit coupling can be neglected in the control design and treated as a disturbance component.

The second section of the paper is devoted to orbit, formation and drag-free dynamics. Orbit dynamics, to be treated in some detail, is formulated as a special kind of the Hill-Clohessy-Wiltshire (shortly HCW) equation [20], [21], which is capable of describing deformation and tilt of the orbit radius. Formation dynamics has been developed on the same path, and is based on the definition of the formation local orbital frame (FLOF). Only the discrete-time embedded model is provided, which is the core of the formation control. Details of the derivation are omitted. To authors' knowledge, equations of this sort are unavailable in the literature. The effort of the literature is mainly devoted to include generic gravity potential terms as in [22] and [23] (which makes accurate the formation free response) or to extend relative orbit motion to highly eccentric orbits as in [24]. Other authors like in [25] adopt orbital element differences. Specifically, in [22] the equations of motion of a generic spacecraft formation in Earth orbit are written via Lagrange's equations, and the generalized equations are shown to reduce to HCW equations [20] under the assumption of a circular reference orbit. In [23] the motion of a spacecraft formation is written in a generic form, as a Hamiltonian dynamic system near a reference solution. The aim is to include J2 and J3 gravity anomalies, but renouncing to drag forces.

Care must be exerted in employing perturbation equations like HCW for control design in the case of a long-distance formation, since significant nonlinear gravity terms are neglected together with higher gravity harmonics. A control authority that neglects them may be demanded an excessive effort. Embedded Model Control fully solves this problem as shown in the Appendix, since it is capable of estimating unknown model errors and of including them in the control law for being rejected. As a further remark, the goal of the present formation control is just to stabilize the mean formation geometry versus long-term drag-free residuals due to accelerometer errors. Such residuals are secular components of the formation variables since their spectral density becomes significant only below the orbit frequency. As such, formation control is designed for leaving intact the formation fluctuations imposed by Earth gravity, which is coherent with a perturbation dynamics like HCW.

Orbit, formation and drag-free control are naturally arranged and designed in a hierarchical way as outlined in Figure 1. Orbit altitude (2D), formation distance and roll/yaw control (the 5D outer loop) provide the long-term reference accelerations to be tracked by 3D drag-free control (the inner loop). Orbit and formation commands are designed to be narrow band, with a bandwidth (BW) well below the orbit frequency close to 0.2 mHz for an orbit altitude around 350 km, not to disturb the mid frequency range where drag free requirements are demanding. A 3D formation control exploiting classical Hill's equations is in Ref. [13].

Experimental (GOCE) and simulated results are shown. Attitude control is not treated, but attitude control is mandatory for minimizing drag-free commands, - the normal of the small front face is kept aligned to the CoM velocity-, and for aligning the satellite-to-satellite line with the laser beam. Attitude and formation control combine in the thruster dispatching law converting the 6D force/torque vector into eight thrusts. Satellite nominal orbits are assumed to be polar, either with the same right ascension of the ascending nodes (in-line formation) or slightly apart to achieve a pendulum formation as in Figure 3.

ORBIT AND FORMATION DYNAMICS

Formation type and frames of reference

Two formation types have been selected as candidates:

1) The formation type A is an in-line formation which consists of a pair of satellites on the same nominal polar orbit, defined by RAAN Ω and perigee anomaly $\varpi \pm \Delta\varpi$, with $|\Delta\varpi| \le 0.015$ rad .

2) The formation type B is a pendulum formation, which consists of a pair of satellites placed on two slightly separated orbits, having either different inclination or right ascension of the ascending node (the latter solution has been selected as preferable). The orbits are defined by RAAN $\Omega \pm \Delta\Omega$ and perigee anomaly $\varpi \pm \Delta\varpi$, with $|\Delta\Omega| \le 0.003$ rad.

The nominal altitude h_{nom} ranges between 325 and 425 km. Orbit period P_{nom}, angular rate ω_{nom} and frequency f_{nom} vary within the range:

$$P_{nom} = 5.46 \div 5.59 \text{ ks},\ \omega_{nom} = 1.12 \div 1.15 \text{ mrad/s},\ f_{nom} = 1.79 \div 1.83 \text{ Hz}. \tag{1}$$

Reference frames

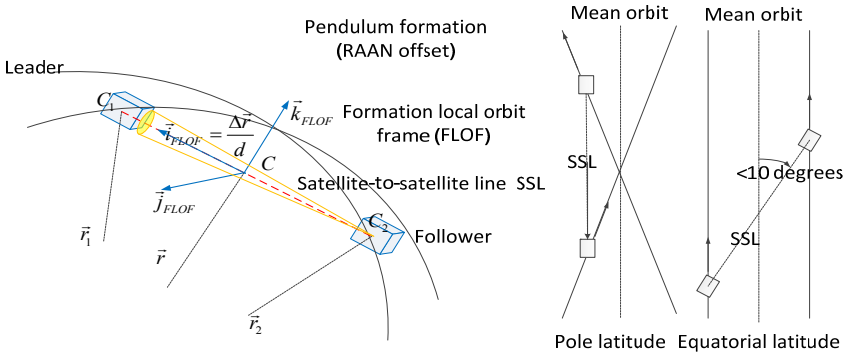

Figure 3 Local and formation frames in the pendulum formation (type B).

Four main frames are necessary. The inertial frame $\mathcal{I} = \{O, \vec{i}_1, \vec{i}_2, \vec{i}_3\}$ is the Earth centered equatorial frame frozen at some date. Two satellites $k = 1, 2$ are considered, where, as in Figure 3, $k = 1$ refers to the leader, and $k = 2$ to the follower. The formation local orbital frame (FLOF) $\mathcal{F} = \{C, \vec{o}_1, \vec{o}_2, \vec{o}_3\}$ is the frame common to both satellites, which is defined by the relative position $\Delta\vec{r} = \vec{r}_1 - \vec{r}_2$ and by the mean radius $\vec{r} = (\vec{r}_1 + \vec{r}_2)/2$ through the relations

$$\begin{aligned} &\vec{o}_1 = \frac{\Delta\vec{r}}{d},\ \vec{o}_2 = \frac{\vec{r}/r \times \Delta\vec{r}/d}{\left|\vec{r}/r \times \Delta\vec{r}/d\right|},\ \vec{o}_3 = \vec{o}_1 \times \vec{o}_2 \\ &d = \left|\Delta\vec{r}\right|,\ r = \left|\vec{r}\right|,\ r_k = \left|\vec{r}_k\right| \end{aligned}. \tag{2}$$

The first axis $\vec{o}_1$ is the direction of satellite-to-satellite line (SSL). The FLOF to inertial transformation R_o^i derives from (2). The third frame is the local vertical local horizontal frame (LVLH) $\mathcal{L}_k = \{C_k, \vec{l}_{k1}, \vec{l}_{k2}, \vec{l}_{k3}\}$ of each satellite and is defined by

$$\vec{l}_3 = \frac{\vec{r}}{r},\ \vec{l}_2 = \frac{\vec{r} \times \dot{\vec{r}}}{\left|\vec{r} \times \dot{\vec{r}}\right|},\ \vec{l}_1 = \vec{l}_2 \times \vec{l}_3. \tag{3}$$

The first axis of the FLOF and LVLH frames is referred to as tangential, the second as lateral and the third one as radial. The fourth frame is the body frame $\mathcal{C}_k = \{C_k, \vec{b}_{k1}, \vec{b}_{k2}, \vec{b}_{k3}\}$ centered in the satellite CoM C_k. The first axis $\vec{b}_{k1}$ is assumed to be aligned with the outcoming laser beam; the third axis $\vec{b}_{k3}$ is aligned with the direction normal to the solar panel plane. The body to inertial transformation is denoted by R_k^i. Nominally, the FLOF frame rotates around $\vec{o}_2$ in both formation types A and B. In the pendulum type it rotates also around $\vec{o}_3$.

Given a coordinate vector, that is to say $\mathbf{r}$, measurement, reference, prediction and tracking error are denoted by $\breve{\mathbf{r}}$, $\underline{\mathbf{r}}$, $\hat{\mathbf{r}}$ and $\tilde{\mathbf{r}} = \underline{\mathbf{r}} - \mathbf{r}$, respectively. The body to formation transformation is denoted by R_k^l and holds

$$R_k^i = R_o^i R_k^o. \tag{4}$$

Orbit and formation perturbations

Consider the CoM dynamics of both satellites

$$\ddot{\vec{r}}_k(t) = -\vec{g}(\vec{r}_k) + \vec{a}_k(t),\ \vec{r}_k(0) = \vec{r}_{k0},\ \dot{\vec{r}}_k(0) = \vec{v}_{k0},\ k = 1,2\,, \tag{5}$$

and transform it into the mean and differential dynamics

$$\begin{aligned} \ddot{\vec{r}}(t) &= -\frac{\vec{g}(\vec{r}_1) + \vec{g}(\vec{r}_2)}{2} + \vec{a}(t),\ \vec{r}(0) = \vec{r}_0,\ \dot{\vec{r}}(0) = \vec{v}_0 \\ \Delta\ddot{\vec{r}}(t) &= -\left(\vec{g}(\vec{r}_1) - \vec{g}(\vec{r}_2)\right) + \Delta\vec{a}(t),\ \Delta\vec{r}(0) = \Delta\vec{r}_0,\ \Delta\dot{\vec{r}}(0) = \Delta\vec{v}_0 \end{aligned}\,. \tag{6}$$

In (5), $\vec{a}_k$ is the non-gravitational acceleration of each satellite, summing up drag-free residuals and orbit/formation authority. Mean and differential non-gravitational accelerations in (6) are defined as

$$\Delta\vec{a} = \vec{a}_1 - \vec{a}_2,\ \vec{a} = \frac{\vec{a}_1 + \vec{a}_2}{2}\,. \tag{7}$$

Orbit perturbations can be expressed in the LVLH frame in two ways (see Figure 4).

1) Hill-Clohessy-Wiltshire [20] perturbations are defined as the CoM displacement $\delta\vec{r}_k = \vec{r}_k - \vec{r}_{nom,k}$ from a Kepler reference orbit $\vec{r}_{nom,k}(t)$ either circular or elliptical [24]. The perturbation coordinates are given in the LVLH frame $\mathscr{S}_{nom,k}$ of the reference orbit.
2) Radial and angular perturbations will be defined and used here. They consist in the radial perturbation $\delta r_k \vec{l}_{3,k} = (r_k - r_{nom,k})\vec{l}_{3,k}$ and in the angular rate $\vec{\omega}_k$ of the orbit LVLH frame $\mathscr{S}$. Since only three degrees-of-freedom exist, the angular rate vector $\vec{\omega}_k$ can only possess two nonzero components. Moreover, if $r_{nom,k}$ is constant, a reference sphere can be defined and the perturbations become the radius deviation δr_k, the deviation $\delta\omega_{y,k}$ of the longitudinal motion expressed by $\omega_{y,k}$, and the lateral perturbation provided by $\omega_{z,k}$.

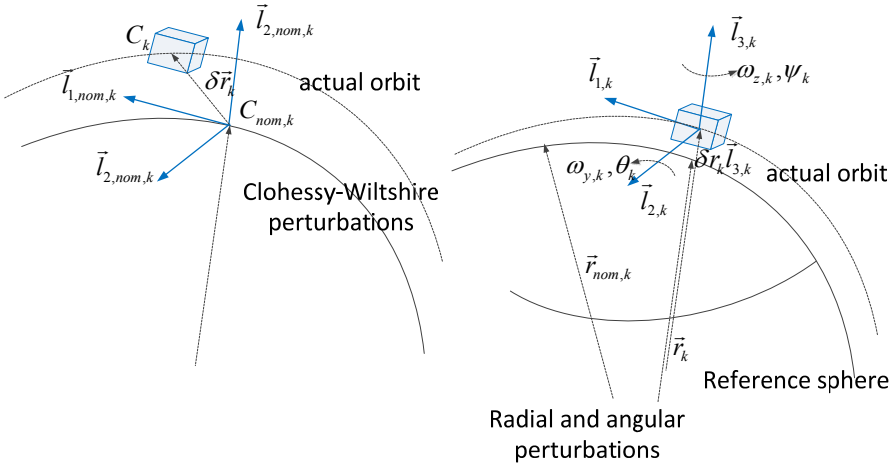

Figure 4 Hill-Clohessy-Wiltshire and radial/angular perturbations.

A combination of Cartesian and angular perturbations can be extended to a two-satellite formation with the help of the FLOF $\mathscr{F}$ which has been defined in (2). A reference sphere of radius r_{nom} is associated to the formation CoM $\vec{r}$, and a nominal formation SSL of length d_{nom} and tangent to the reference sphere is associated to the relative position $\Delta\vec{r}$. Three Cartesian perturbations $(\delta d, \delta r_x, \delta r_z)$ are defined as follows (see Figure 5)

$$\begin{aligned} \Delta\vec{r} &= (d_{nom} + \delta d)\vec{o}_1 \\ \vec{r} &= (r_{nom} + \delta r_z)\vec{o}_3 + \delta r_x \vec{o}_1 \end{aligned}\,. \tag{8}$$

The perturbation δr_x is referred to as 'radial difference' since it is proportional to the mean radius difference of the satellite orbits. The other three DoF are provided by the angular rate vector $\vec{\omega}$ of

the FLOF, that now can be shown to possess three nonzero components. The paper restricts to a detailed derivation of the orbit perturbation equations.

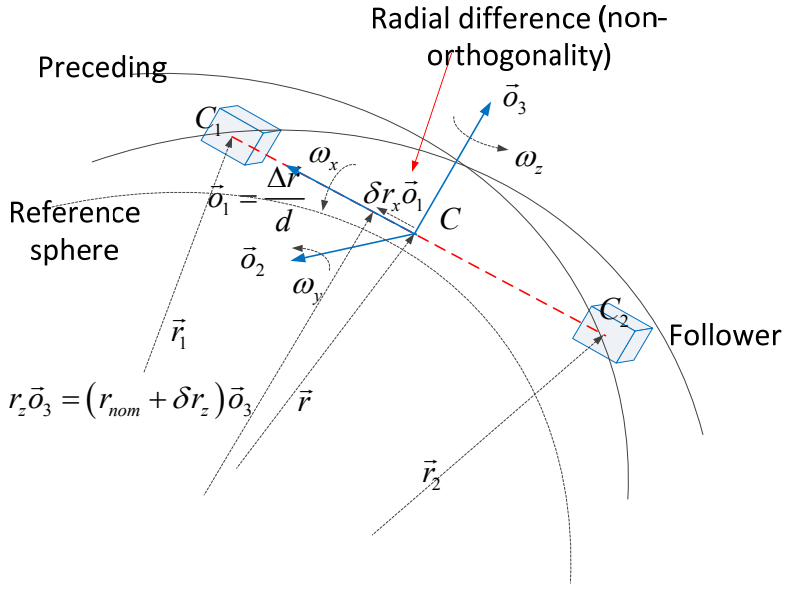

Figure 5 Formation perturbations.

The perturbations in (8) with respect to a reference sphere fits to a type A formation, but not to the type B, since the reference orbit of the formation CoM is circular for the type A, but elliptical for the type B. Actually the difference is proved to be negligible. In fact the plane of the elliptical orbit is shown to coincide with the plane of the type A less a negligible deviation, and the mean radius of the elliptical orbit - in other terms the semi-major axis - is the same as for the type A. Since the requirements of the formation control in Table 1 only concern secular deviations below the orbit angular rate, the reference elliptical orbit can be replaced by the mean circular orbit. In summary, perturbations (8) apply also to type B.

Let us assume that the reference circular orbits $\vec{r}_{nom,k}$ of each satellite have equal and constant radiuses $r_1 = r_2 = \rho$. The inertial coordinates hold

$$\mathbf{r}_{nom,k}(t) = \rho Z(\Omega) \begin{bmatrix} \cos(\Delta\Omega)\cos(\theta(t) \pm \Delta\varpi) \\ \pm\sin(\Delta\Omega)\cos(\theta(t) \pm \Delta\varpi) \\ \sin(\theta(t) \pm \Delta\varpi) \end{bmatrix}, \qquad (9)$$
$$\theta(t) = \varpi + \omega_{nom} t, \ \omega_{nom} = \sqrt{\mu / \rho^3}$$

where $Z(\Omega)$ denotes a rotation around $\vec{i}_3$, and the numerical range of ω_{nom} is reported in (1). Using (9) the next Lemma is proved.

Lemma 1. The reference orbit of the formation CoM $\vec{r}_{nom} = (\vec{r}_{1,nom} + \vec{r}_{2,nom})/2$ is circular for the formation type A and elliptical for the formation type B, has a semi-major axis $a_{nom} < \rho$, and has the angular rate ω_{nom} in (9).

Proof. The angular rate is written by taking the average of the two orbits as follows

$$\ddot{\vec{r}}_{nom,k}(t) = \frac{\mu}{\rho^3}\vec{r}_{nom,k}(t), \ k = 1,2$$
$$\ddot{\vec{r}}_{nom}(t) = \frac{\ddot{\vec{r}}_{nom,1}(t) + \ddot{\vec{r}}_{nom,2}(t)}{2} = \frac{\mu}{\rho^3}\vec{r}_{nom}(t) \qquad (10)$$

The orbit shape is obtained by transforming (9) into orbit plane components (perigee frame), which yields

$$\mathbf{r}_{nom}(t) = \rho\cos(\Delta\varpi)Z(\Omega)X(\pi/2+\Delta i)\begin{bmatrix}\cos(\Delta\Omega)\cos\theta(t)\\ \sqrt{1+\tan^2(\Delta i)}\sin\theta(t)\\ 0\end{bmatrix}, \qquad (11)$$

$$\tan\Delta i = -\sin(\Delta\Omega)\tan(\Delta\varpi),\ |\tan\Delta i| \le 0.05 \text{ mrad}$$

where Δi is the negligible inclination correction. For the type A, $\Delta\Omega = 0$ and the orbit is circular with radius $a_{nom} = \rho\cos(\Delta\varpi)$. For the type B, the orbit is elliptical with eccentricity $e \cong |\Delta\Omega| \le 0.003$. By neglecting Δi, the semi-major axis holds $a_{nom} \cong \rho\cos(\Delta\varpi)$. □

As a corollary of Lemma 1, the reference orbit of Type B can be approximated by the same circular polar orbit of the type A. This follows by neglecting Δi and $e \cong |\Delta\Omega|$. More precisely, $\mathbf{r}_{nom}$ of type A coincides with the mean circular orbit of type B. This follows by expressing the radius in terms of the eccentric anomaly E and by taking the orbit average as

$$|\mathbf{r}_{nom}(t)| = a_{nom}(1-e\cos E(t))$$
$$\frac{1}{P_{nom}}\int_t^{t+P_{nom}} |\mathbf{r}_{nom}(\tau)|\,d\tau = a_{nom}\ , \qquad (12)$$

where P_{nom} has been defined in (1). Observe that whereas the error of neglecting Δi is well less than 1m, the radius fluctuation in (12) due to e is of the order of 10 km. A goal of the orbit and formation control is to leave intact periodical components, but to cancel secular components.

Orbit perturbation dynamics

Continuous time equations

In this section, equations imposed by radial and angular perturbations are derived and compared with HCW equations that can be found in [13]. We restrict to a single satellite and the subscript k is dropped. The LVLH frame $\mathcal{S}$ is the frame of reference. To the purpose, let us decompose the orbit radius in (5) as

$$\vec{r} = r\vec{l} = (r_{nom} + \delta r)\vec{l}_3,\ r_{nom} = \text{constant}\ , \qquad (13)$$

and the components of the LVLH angular rate vector as $\vec{\omega} = \omega_x\vec{l}_1 + \omega_y\vec{l}_2 + \omega_z\vec{l}_3$. The following lemma is well known and expresses the alignment of the orbit angular momentum with the LVLH second axis $\vec{l}_2$.

Lemma 2. The longitudinal component of $\vec{\omega}$ is zero, $\omega_x = 0$. □

Lemma 2 implies that the orbit deviation from the instantaneous plane $(\vec{l}_1, \vec{l}_3)$ can only be obtained through a rotation ψ of the horizontal axis $\vec{l}_1$ - in other terms of the velocity vector $\dot{\vec{r}}$ - on the reference sphere. The perturbation equations to be derived below will reinforce the statement. To this end, gravity vector $\vec{g}$ in (5) splits into a (variable) radial component and a perturbation $\delta\vec{g}$:

$$\vec{g}(\vec{r}) = \omega_s^2(t)r(t)\vec{l}_3 + \delta\vec{g}(r,\theta)$$
$$\delta\vec{g}(r,\theta) = \delta g_x(r,\theta)\vec{l}_1 + \delta g_y(r,\theta)\vec{l}_2 + \delta g_z(r,\theta)\vec{l}_3\ . \qquad (14)$$
$$\omega_s^2(t) = \mu/r^3(t)$$

In principle also the J2 gravity term should be made explicit in (14), since as shown in [13], orbital frequencies modify of the order of 0.1 % and long term beat motions are generated. Model derivation including J2 will be a development of this study, but the present model has been shown by extensive simulations to be effective for control design also without an explicit inclusion of J2 corrections.

The vectorial equation of the perturbed motion of (5) follows from the derivative of $\vec{r}$ in (13) and holds

$$\delta\ddot{\vec{r}}_3 = -\dot{\vec{\omega}} \times \vec{r} - \vec{\omega} \times \left(\vec{\omega} \times \vec{r}\right) - 2\vec{\omega} \times \delta\dot{\vec{r}}_3 + \vec{a} + \vec{g}\left(\vec{r}\right). \tag{15}$$

The LVLH components write as follows

$$\begin{aligned}
&\vec{l}_1: \ \dot{\omega}_y(t) = -2\omega_y(t)\delta\dot{r}(t)/r + a_x(t)/r + \delta g_x\left(r, \theta(t)\right)/r \\
&\vec{l}_2: \ \omega_z(t) = \left(\omega_y(t) r(t)\right)^{-1}\left(a_y(t) + \delta g_y\left(r, \theta(t)\right)\right) \\
&\vec{l}_3: \ \delta\dot{v}_r(t) = \left(\omega_y^2(t) - \omega_s^2(r)\right) r(t) + a_z(t) + \delta g_z\left(r, \theta(t)\right)
\end{aligned} . \tag{16}$$

Equation (16) describes the perturbation dynamics, since it is driven by the exogenous acceleration a_k. It must be completed with kinematic equations. They are derived by denoting the Euler angles as $(\varphi, \vartheta = \theta + \delta\theta, \psi)$, where θ has been defined in (9), and by adopting the 231 Tait-Bryan sequence, as follows

$$\begin{aligned}
&\delta\dot{r}(t) = \delta v_r(t) \\
&\begin{bmatrix} \dot{\varphi} \\ \dot{\vartheta} \\ \dot{\psi} \end{bmatrix}(t) = \begin{bmatrix} -\cos\varphi\tan\psi & \sin\varphi\tan\psi \\ \cos\varphi/\cos\psi & -\sin\varphi/\cos\psi \\ \sin\varphi & \cos\varphi \end{bmatrix} \begin{bmatrix} \omega_y \\ \omega_z \end{bmatrix}.
\end{aligned} \tag{17}$$

By dropping the second equation from (16) and replacing ω_z in (17), the seven equations in (16) and (17) reduce to six like HCW equation. The angular rate ω_x has been dropped because of Lemma 2.

Because of the orbit control, small perturbations can be assumed in (16) and (17), and the perturbation dynamics can be linearized. The next Lemma states that the equilibrium point on the reference sphere provides a circular orbit as in the HCW assumption.

Lemma 3. The equilibrium point on the reference sphere $r = r_{nom}$ holds

$$\begin{aligned}
&\omega_{xe} = \omega_{ze} = 0 \\
&\omega_{ye} = \omega_{nom} = \omega_s\left(r_{nom}\right) \\
&\delta\dot{r}_e = 0, \ \delta r_e = 0 \\
&\dot{\vartheta}_e = \dot{\theta} = \omega_{nom} \\
&\psi_e = 0 \\
&\varphi_e = 0
\end{aligned} . \tag{18}$$

Proof. It follows by setting $\delta g_k = a_k = 0$ in (16), and by zeroing the derivatives in (16) and in (17), except ϑ. □

It is now possible to write the linearized equations around the equilibrium (18). A sixth order state equation is obtained having the following state vector, whose components possess length and angular units; namely

$$\begin{aligned}
&\delta\mathbf{x}(t) = \begin{bmatrix} \delta r \\ \delta v = \delta\dot{r}/\omega_{nom} \\ \delta s = 2\delta r + r_{nom}\delta\omega_y/\omega_{nom} \\ \delta x = \delta\theta r_{nom} = \left(\vartheta - \theta\right) r_{nom} \\ \delta y = \psi r_{nom} \\ \delta z = \varphi r_{nom} \end{bmatrix}. \\
&\delta\omega_y = \omega_y - \omega_{nom}
\end{aligned} \tag{19}$$

The first entry in (19) is the radial perturbation and δv is the normalized radial rate, δx is the tangential perturbation and δs is the total longitudinal speed, δy and δz are the lateral perturbations. To write the linearized equation, the external acceleration components a_j, $j = x, y, z$ in (15) are split into command u_j and disturbance d_j, where the latter correspond to the drag-free residuals. The measurement y_r is the radial perturbation which is affected by the model error e_r. The next lemma is immediate.

Lemma 4. The linearized state equation of (16) and (17) around the equilibrium (18) takes the form

$$\begin{bmatrix} \delta\dot{r} \\ \delta\dot{v} \\ \delta\dot{s} \\ \delta\dot{x} \\ \delta\dot{y} \\ \delta\dot{z} \end{bmatrix}(t) = \omega_{nom} \left[\begin{array}{ccc|ccc} 0 & 1 & 0 & 0 & 0 & 0 \\ -1 & 0 & 2 & 0 & 0 & 0 \\ 0 & 0 & 0 & 0 & 0 & 0 \\ \hline -2 & 0 & 1 & 0 & 0 & 0 \\ 0 & 0 & 0 & 0 & 0 & 1 \\ 0 & 0 & 0 & 0 & -1 & 0 \end{array}\right] \begin{bmatrix} \delta r \\ \delta v \\ \delta s \\ \delta x \\ \delta y \\ \delta z \end{bmatrix}(t) + \frac{1}{\omega_{nom}} \left[\begin{array}{ccc} 0 & 0 & 0 \\ 1 & 0 & 0 \\ 0 & 1 & 0 \\ \hline 0 & 0 & 0 \\ 0 & 0 & 1 \\ 0 & 0 & 0 \end{array}\right] \begin{bmatrix} u_z + d_z + \delta g_z \\ u_x + d_x + \delta g_x \\ \hline u_y + d_y + \delta g_y \end{bmatrix}. \tag{20}$$

The radial perturbation δr is controllable by both radial and longitudinal commands u_z and u_x. □

The equation matrices of (20) are the same as the HCW equation in [13] upon reordering of the state variables. The main difference lies in the separation between radial and angular perturbations as expressed by (19). This is coherent with the NGGM control objectives: (i) orbit altitude control through δr, (ii) alignment of the body quaternion to the orbit frame quaternion made by attitude control.

If we restrict to altitude control, only the radial perturbation is measured from GNSI instruments as follows

$$\begin{aligned} y_r(t) &= \begin{bmatrix} 1 & 0 & 0 & 0 & 0 & 0 \end{bmatrix} \delta\mathbf{x}(t) + e_r(t) \\ y_r(t) &= r(t) - r_{nom} \end{aligned}, \tag{21}$$

where e_r is the model error, including measurement errors and neglected dynamics.

Discrete-time orbit dynamics

In the GOCE mission [27], the average orbit height was regulated tangentially through the unique longitudinal thruster. The height was regulated from ground station to stay within average fluctuations of about 10 m. By disposing of a six-DoF propulsion, both command authorities become available according to Lemma 4. GOCE regulation was obtained by impulsive commands, which is a standard orbit control practice. Here we look for a continuous control which is capable of respecting the drag-free requirements. A candidate is a stepwise command with a sampling time equal to the orbit period P_{nom}, or even a piecewise command that linearly interpolates two successive values and is sampled at a shorter time $T_p = P_{nom} / N_p$, with $N_p > 1$. Four main reasons can be given.

1) The sampling frequency f_{nom} is well below the critical drag-free BW, $f_{nom} \cong 0.2$ mHz<1 mHz .
2) Only the secular disturbance components d_j in (20) must be cancelled, without affecting the periodic terms δg_j.
3) A stepwise (piecewise) command has a smaller magnitude than an impulsive control and the spectrum is decaying with a -20 dB/decade (-40 dB/decade).
4) The baseline thruster authority is rather small, of the order of a few millinewtons, and only a portion can be allocated to orbit control.

A first issue is whether the controllability of the state equation (20) is conserved, when converted to discrete time under the orbit sampling step P_{nom}. Since the HCW equation and the radial/angular equation (20) are equivalent, we shall restrict to the latter.

A second issue concerns the aliasing of the periodic gravity components δg_j in (20), which may generate parasitic secular components having magnitude larger than the command authority. This issue is solved by filtering the measurements through a suitable notch filter having Bode magnitude as in Figure 6. Filter dynamics will not enter the Embedded Model to be derived below, thus contributing to neglected dynamics. To partially overcome the drawback, the notch filter transfer function has been designed to bounded by a delay less than $P_{nom}/2$, and the closed-loop eigenvalues of the altitude control have been tuned on such account. As a result the residual contribution of δg_j comes only from the Earth rotation rate and from the inaccuracy of P_{nom}. Therefore the term δg_j can be dropped from equation (20) and the residuals can be hidden in the term d_j.

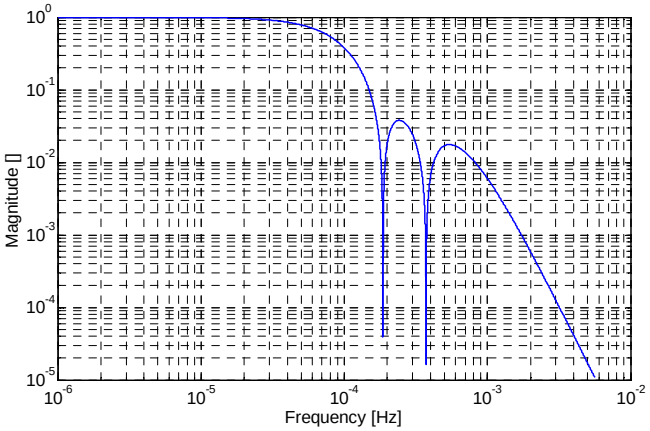

Figure 6 Typical Bode magnitude of the notch filter.

The discrete-time (DT) equation of (20), sampled at the orbit period P_{nom} and assuming zero-order interpolation (stepwise) along each orbit period, can be proved to have the form

$$\begin{bmatrix} \delta r \\ \delta v \\ \delta s \\ \delta x \\ \delta y \\ \delta z \end{bmatrix}(n+1) = \left[\begin{array}{ccc|ccc} 1 & 0 & 0 & 0 & 0 & 0 \\ 0 & 1 & 0 & 0 & 0 & 0 \\ 0 & 0 & 1 & 0 & 0 & 0 \\ \hline 0 & 0 & -6\pi & 1 & 0 & 0 \\ 0 & 0 & 0 & 0 & 1 & 0 \\ 0 & 0 & 0 & 0 & 0 & 1 \end{array}\right] \begin{bmatrix} \delta r \\ \delta v \\ \delta s \\ \delta x \\ \delta y \\ \delta z \end{bmatrix}(n) + \frac{2\pi}{\omega_{nom}^2} \left[\begin{array}{cc|c} 0 & 2 & 0 \\ 0 & 0 & 0 \\ 0 & 1 & 0 \\ \hline -2 & -3 & 0 \\ 0 & 0 & 0 \\ 0 & 0 & 0 \end{array}\right] \left[\begin{array}{c} u_z + d_z \\ u_x + d_x \\ \hline u_y + d_y \end{array}\right](n). \qquad (22)$$

Equation (22), which applies also to HCW equation in [13], can be referred to as a secular orbit dynamics. The frequency domain is upper bounded by the Nyquist frequency $f_{\max} = 0.5/P_{nom}$. The link between $t_n = nP_{nom}$ and the faster sampling times $t_i = iT$, where $T = 0.1$ s is the accelerometer time unit, which is the least AOCS time unit, is given by

$$n(i) = \text{floor}(i/N),\ N = \text{round}(P_{nom}/T). \qquad (23)$$

All the state variables are decoupled except the lateral perturbation pair δy and δz. The input variables u_j and d_j are given in acceleration units $\left[\text{m/s}^2\right]$. The next Lemma fixes the controllability properties. We are only interested in radial controllability. We assume that the body axes are aligned with LVLH axes.

Lemma 5. The radial perturbation is only tangentially controllable, by u_x. The longitudinal perturbation δx is both tangentially and radially controllable. The lateral perturbations δy and δz, which are proportional to angular perturbations, are not controllable. The radial dynamics expressed by δr is bounded-input-bounded output (BIBO) unstable. □

Since we are only interested in the radial (altitude) control, we drop the uncontrollable state variables and the radial command from (22), but, in order to describe the secular components (bias

and drift) of the unknown disturbance d_j, where $j = x, z$, we add two first-order stochastic dynamics having state variable x_{dj}. The assumptions lead to the following embedded model of the orbit

$$\begin{bmatrix} \delta r \\ \delta s \\ \delta x \\ x_{dx} \\ x_{dz} \end{bmatrix}(n+1) = \begin{bmatrix} 1 & 0 & 0 & 2b & 0 \\ 0 & 1 & 0 & 1 & 0 \\ 0 & -6\pi & 1 & -3 & -2 \\ 0 & 0 & 0 & 1 & 0 \\ 0 & 0 & 0 & 0 & 1 \end{bmatrix} \begin{bmatrix} \delta r \\ \delta s \\ \delta x \\ x_{dx} \\ x_{dz} \end{bmatrix}(n) + \begin{bmatrix} 2b & 0 & 0 & 0 \\ b & 0 & 0 & 0 \\ -3b & -2b & 0 & 0 \\ 0 & 0 & 1 & 0 \\ 0 & 0 & 0 & 1 \end{bmatrix} \begin{bmatrix} u_x + w_x \\ u_z + w_z \\ w_{dx} \\ w_{dz} \end{bmatrix}(n) \quad . \tag{24}$$

$$y_r(n) = \begin{bmatrix} 1 & 0 & 0 & 0 & 0 \end{bmatrix} \begin{bmatrix} \delta r \\ \delta s \\ \delta x \\ x_{dx} \\ x_{dz} \end{bmatrix}(n) + e_r(n)$$

where

$$b = \frac{P_{nom}^2}{2\pi} = \frac{2\pi}{\omega_{nom}^2}. \tag{24}$$

In (24) w_x, w_{dx} and w_z, w_{dz} play the role of arbitrary, but bounded signals, to be kept as unpredictable and zero mean. They are due to the filtered wide-band components of the drag-free residuals (bias and drift of the accelerometer are expressed by the state x_{dx}). Denote the wide-band unilateral root Power Spectral Density (briefly PSD) of w_j by S_{wj}. We assume the latter to be constant - like for a discrete-time white noise-, because notch filter in Figure 6 plays the role of an anti-aliasing filter. Then the standard deviation of w_j can be approximated by

$$\sigma_{wj} \cong S_{wj} / \sqrt{P_{nom} / 2} \cong 0.01 \omega_{nom}^2 \sqrt{P_{nom}} \ \text{m/s}^2 . \tag{25}$$

Discrete-time formation dynamics

In the NGGM mission, the altitude control can be either separately implemented on each satellite, or combined with the formation control. The former solution applies to the early mission phases when formation is still under construction and each satellite is stand-alone controlled. As soon as the formation distance can be on-board controlled (it requires radio interlink to exchange GNSI data), altitude and formation control are combined into a unique strategy. This is permitted by the FLOF definition in (2) and by the perturbation definition in (8) and in Figure 5.

Formation dynamics is obtained by the same method for the orbit dynamics. The degrees of freedom now become six and the corresponding state equations twelve. A detailed derivation and proof would require an ad hoc paper. Here only the discrete-time embedded model is reported together with the control law. To simplify treatment only the three DoF of interest as in (8) are reported, namely the distance perturbation δd, the normalized 'radial difference' $\delta \rho_x$ and the radial perturbation δr_z:

$$\begin{aligned} \delta d &= d - d_{nom} \\ \delta \rho_x &= -\alpha \delta r_x \cong r_2 - r_1 \\ \delta r_z &= r_z - r_{nom} \\ \alpha &= d_{nom} / r_{nom} \le 0.04 \end{aligned} , \tag{26}$$

where d_{nom} is the mean reference distance. The discrete-time state equation that has been obtained by discretizing a continuous-time perturbation equation at the orbit nominal period P_{nom}, was found to hold

$$\begin{bmatrix}\delta d\\ \delta\rho_x\\ \delta r_z\end{bmatrix}(n+1)=\begin{bmatrix}1 & 3\pi & 0\\ 0 & 1 & 0\\ 0 & 0 & 1\end{bmatrix}\begin{bmatrix}\delta d\\ \delta\rho_x\\ \delta r_z\end{bmatrix}(n)+b\begin{bmatrix}3\pi & 2 & 0\\ 2 & 0 & 0\\ 0 & 0 & 2\end{bmatrix}\left(\mathbf{v}(n)+\mathbf{d}(n)\right)+\begin{bmatrix}3\pi\\ 0\\ 0\end{bmatrix}\delta w(n)$$
$$\delta w=2\dot r_z/\omega_{nom}-\left(2\dot d/\omega_{nom}+3\alpha\delta r_x\right)$$
$$\mathbf{v}+\mathbf{d}=\begin{bmatrix}\Delta u_x-\alpha u_z+\Delta d_x-\alpha d_z\\ \Delta u_z+\Delta d_z\\ u_x+d_x\end{bmatrix} \tag{27}$$
$$b=\frac{2\pi}{\omega_{nom}^2}$$

The time step n has the same meaning as in (23). The command entries may be expressed in terms of the satellite commands using $k=1,2$ to indicate leader and follower satellites:

$$\begin{aligned}&\Delta u_j=u_{j2}-u_{j1},\ j=x,z\\ &u_j=\left(u_{j1}+u_{j2}\right)/2\end{aligned} \tag{28}$$

Observe that the difference in (28) is the opposite of that adopted in (7), but it allows negative sign elimination. In matrix form we have

$$\mathbf{v}=S\mathbf{u}=\begin{bmatrix}-1 & -\alpha/2 & 1 & -\alpha/2\\ 0 & -1 & 0 & 1\\ 1/2 & 0 & 1/2 & 0\end{bmatrix}\mathbf{u},\ \mathbf{u}=\begin{bmatrix}u_{x1}\\ u_{z1}\\ u_{x2}\\ u_{z2}\end{bmatrix} \tag{29}$$

A similar definition applies to Δd_j and d_j, $j=x,z$. Only the longitudinal and radial commands enter (27). The input term δw in (27) is the sum of two DC terms, since the corresponding variables can be shown to be the free response of a single integrator. Therefore, the second term within brackets says that the mean distance rate $\dot d$ is proportional to the 'radial difference' $\delta\rho_x$. In fact, equation (27) shows that $\delta\dot d$ is driven by $\delta\rho_x$, and the latter is proportional to $\dot d$. Equation (27) can be rewritten in the compact form

$$\begin{bmatrix}\mathbf{x}_c\\ \mathbf{x}_d\end{bmatrix}(n+1)=\begin{bmatrix}A_c & I\\ 0 & I\end{bmatrix}\begin{bmatrix}\mathbf{x}_c\\ \mathbf{x}_d\end{bmatrix}(n)+\begin{bmatrix}B_cS\\ 0\end{bmatrix}\mathbf{u}(n)+\begin{bmatrix}\mathbf{w}\\ \mathbf{w}_d\end{bmatrix}(n),\ \begin{bmatrix}\mathbf{x}_c\\ \mathbf{x}_d\end{bmatrix}(0)=\begin{bmatrix}\mathbf{x}_{c0}\\ \mathbf{x}_{d0}\end{bmatrix}$$
$$\mathbf{y}(n)=\begin{bmatrix}I & 0\end{bmatrix}\begin{bmatrix}\mathbf{x}_c\\ \mathbf{x}_d\end{bmatrix}(n)+\mathbf{e}(n) \tag{30}$$
$$\mathbf{d}(n)=\mathbf{x}_d(n)+\mathbf{w}(n)$$

In (30), $\mathbf{x}_c$ is the controllable state vector, A_c is the state matrix and B_c is the command matrix in (27) The disturbance vector $\mathbf{d}$, which includes also the bias $G_c\delta w$, has been split into the state $\mathbf{x}_d$ and the noise $\mathbf{w}$. The state vector $\mathbf{x}_c$ is directly measurable from GNSI data through a notch filter, less the model error $\mathbf{e}$. The following Lemma indicates that (30) is overactuated, and command optimization is possible through a pseudo-inverse.

Lemma 6. The matrix $B=B_cS$ in (30), sized 3×4, is full rank and admits the pseudo inverse

$$B^\dagger=S^\dagger B_c^{-1}=S^T\left(SS^T\right)^{-1}B_c^{-1}.\square \tag{31}$$

Drag-free discrete-time dynamics

Orbit and formation embedded models (24) and (30) assume that high-frequency ($f>f_{nom}=1/P_{nom}$) forcing accelerations in (20) are only due to the gravity periodic components

δg_k. This is only true if short-term non-gravitational accelerations are cancelled by an appropriate control action, referred to as drag-free control. Cancellation should not concern orbit and formation authority, as they are designed to be low-frequency, $f < f_{nom}$. Cancellation can be formulated as a tracking problem, where the measured non-gravitational acceleration tracks a reference acceleration a_{ref} imposed by orbit and formation control. Such an acceleration has been specifically denoted by u_x and u_z in (22) (the subscript k was dropped), and by u_{xk} and u_{zk}, $k = 1,2$, in (29). In essence, reference accelerations consist of the opposite of the accelerometer bias and drift, as they corrupt drag-free commands, but are estimated from GNSI measurements and are rejected by orbit and formation commands.

Assume that linear accelerometers provide measurements in the body frame $\mathcal{C}_k$. Since attitude control is such to align body frame to FLOF frame $\mathcal{F}$ with accuracy of the order of microradians, accelerations can be assumed to be measured in the FLOF frame. Since drag-free control is actuated on each satellite, a single satellite is considered, dropping the subscript k. The embedded model allows each FLOF component to be controlled separately, leading to three decoupled drag-free controls for each spacecraft. To this end, denote a generic scalar measurement with y_a and the corresponding non-gravitational acceleration with a. Measurements being sampled, a discrete time $t_i = iT$ is adopted, $T = 0.1$ s being the accelerometer time unit in (23). y_a and a are decomposed as follows

$$\begin{aligned} a(i) &= u_a(i) + d_a(i) \\ y_a(i) &= a(i) + b_a(i) + w_a(i) \end{aligned}, \tag{32}$$

where u_a is the command, d_a is the disturbance to be cancelled, b_a is the accelerometer bias/drift and w_a is the short-term error. The following Theorem tells how to model d_a.

Theorem 1. Assume d_a is completely unknown and that no relation is known with any variable except y_a in (32). To make d_a be exactly cancelled at any instant (ideal drag-free) such as $a(i) = 0$ in (32), d_a must be the output of a state equation driven the accelerometer measurements.

Proof. The disturbance d_a can only be derived from y_a either through a static or dynamic relation. Assuming $a(i) = 0$, a static relation may only replace d_a with the accelerometer error. Therefore only a dynamic relation is viable. Traditionally this is done by integrating accelerometer measurements. The Embedded Model Control [15], [16], [28] implements a more generic procedure, by constructing the stochastic dynamic model of the disturbance class to be estimated and rejected. □

Assuming full uncertainty, the disturbance dynamics can only be driven by arbitrary unknown signals to be designed [26]. Their design has exploited experimental data and literature about thermosphere density at altitudes from 300 to 400 km and in a frequency band from DC up to 1 Hz as requested by drag free requirements. Experimental thruster noise has been also accounted for. A second-order stochastic dynamics driven by a three-dimensional bounded noise vector $\mathbf{w}_d$ allows to envelope the high-frequency spectral density of combination of drag, thruster noise and accelerometer bias/drift [14]. The relevant state equation which includes sensor and actuator dynamics and is embedded in the control unit, reads as

$$\begin{aligned} &\mathbf{x}_d(i+1) = A_d\mathbf{x}_d(i) + B_d u(i) + G_d\mathbf{w}_d(i),\ \mathbf{x}_d(0) = \mathbf{x}_{d0} \\ &y_a(i) = C_d\mathbf{x}_d(i) + e_a(i) \\ &d_a(i) + b_a(i) = x_d(i) + w_d(i) \\ &a(i) = d_a(i) + b_a(i) + u_a(i) \end{aligned}. \tag{33}$$

Notations in (33) are as follows

$$A_d = \begin{bmatrix} 1-\beta_d & \beta_d & 0 \\ 0 & 1 & 1 \\ 0 & 0 & 1 \end{bmatrix},\ B_d = \begin{bmatrix} \beta_d \\ 0 \\ 0 \end{bmatrix},\ G_d = \begin{bmatrix} 1 & 0 & 0 \\ 0 & 1 & 0 \\ 0 & 0 & 1 \end{bmatrix},\ \mathbf{x}_d = \begin{bmatrix} x_a \\ x_d \\ s_d \end{bmatrix},\ \mathbf{w}_d = \begin{bmatrix} w_a \\ w_d \\ w_s \end{bmatrix}. \quad (34)$$

$$C_d = \begin{bmatrix} 1 & 0 & 0 \end{bmatrix}$$

Disturbance d_a and bias/drift b_a sum up in the third equation of (33), since bias cannot be separated from accelerometer data. Actuator and sensor dynamics is accounted for by a first-order dynamics (first row in (33)) as in the GOCE drag-free control [14]. Drag-free control is designed upon and includes (33). The variable e_a is the model error. The fourth equation in (33) provides the acceleration a that has to be zeroed. For GOCE-class accelerometers and thrusters, sensor and actuator dynamics in (33) simplifies to a delay, i.e. $\beta_d = 1$. The next Lemma certifies that (33) agrees with Theorem 1.

Lemma 7. Equation (33) is observable from y_a.

ORBIT AND FORMATION CONTROL

As already mentioned orbit and formation control are organized in a hierarchical way. The inner loop is the drag-free control; the outer loop is the orbit/formation control. The block diagram is in Figure 7. Only the formation control is reported here. The orbit control is a simplification of the formation control when each satellite is stand-alone controlled. Both algorithms are organized around an embedded model, which is fed by noise estimator and control law. Drag-free control is the simpler one, since no reference generator is necessary. Formation control includes the reference generator which matches reference signals and reference model, and thus provides reference trajectory and command. The preprocessing blocks convert measurements into embedded-model output variables. Formation preprocessing is followed by notch filters that eliminate the orbit periodic terms not to be touched. The notch filter output is then sampled at the orbit rate. Formation preprocessing and notch filter work at the GNSI time unit $T_g = 1$ s.

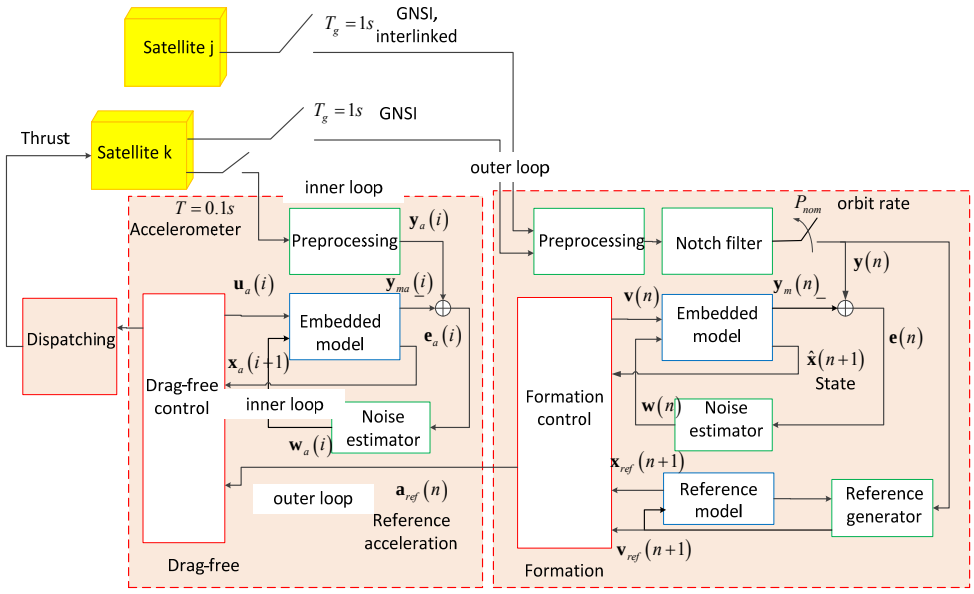

Figure 7 Block-diagram of the formation and drag free control

Control objectives and hierarchy

Ideal control objectives are the following.

1) Drag-free. The total non-gravitational acceleration of each satellite and of each FLOF coordinate must track the orbit and formation acceleration a_{ref}:

$$a = a_{ref} . \tag{35}$$

2) Formation. The long-term distance must be constant:

$$d_{ave}(t) = \int_{t-P_{nom}}^{t} d(\tau) d\tau = d_{nom} . \tag{36}$$

3) Orbit. The long-term altitude must be constant:

$$r_{ave}(t) = \int_{t-P_{nom}}^{t} r(\tau) d\tau = r_{nom} . \tag{37}$$

Actually, drag-free requirements are expressed in terms of a bowl-shape upper limit $\bar{S}_a(f)$ of the spectral density of a, as in Figure 2, whose minimum insists on the frequency band

$$\mathscr{B} = \left\{ 1\ \text{mHz} \cong 5\underline{f} \le f \le 0.1\ \text{Hz} \right\} . \tag{38}$$

In (38) the upper frequency limit matches the Earth ground spatial resolution of 100 km. At low Earth orbits, that is to say at the altitudes from 325 to 425 km, drag rejection up to $f_d \cong 0.5\ \text{Hz}$ is mandatory if such a spatial resolution [14] should be achieved. That is made possible by an accelerometer bandwidth wider than the Nyquist frequency of 5 Hz. Orbit control must be multi-rate and hierarchical. The low-frequency increase of $\bar{S}_a(f)$ in Figure 2 allows the residual acceleration to accommodate a_{ref} which is in charge of cancelling accelerometer bias/drift.

Orbit altitude control

The reference trajectory

The reference dynamics is the same as in (24), but free of noise and disturbance. Its role is to compute a smooth reference trajectory of the radial perturbation, which is driven by a bounded command authority. The reference dynamics holds:

$$\begin{bmatrix} \delta r_{ref} \\ \delta s_{ref} \\ \delta x_{ref} \end{bmatrix}(n+1) = \begin{bmatrix} 1 & 0 & 0 \\ 0 & 1 & 0 \\ 0 & -6\pi & 1 \end{bmatrix} \begin{bmatrix} \delta r_{ref} \\ \delta s_{ref} \\ \delta x_{ref} \end{bmatrix}(n) + b \begin{bmatrix} 2 & 0 \\ 1 & 0 \\ -3 & -2 \end{bmatrix} \begin{bmatrix} u_{x,ref} \\ u_{z,ref} \end{bmatrix}(n), \quad \begin{bmatrix} \delta r_{ref} \\ \delta s_{ref} \\ \delta x_{ref} \end{bmatrix}(0) = \begin{bmatrix} \delta r_{0,ref} \\ \delta s_{0,ref} \\ \delta x_{0,ref} \end{bmatrix} . \tag{39}$$

Given an initial, measured radial perturbation $\delta r_{0,ref} = r - r_{nom}$, and the command bound $|u_x| \le u_{x,\max}$, the reference command is computed as follows

$$\begin{aligned} u_{x,ref}(n) &= \text{sat}\left(-k_{ref} \delta r_{ref}(n) / \left(2bu_{x,\max} \right) \right) u_{x,\max} \\ u_{z,ref}(n) &= 0 \\ \text{sat}(x) &= \begin{cases} -1, & x < -1 \\ x, & |x| \le 1 \\ 1, & x > 1 \end{cases} \end{aligned} \tag{40}$$

The next Theorem provides conditions for closed-loop stabilization of (39) and (40).

Theorem 2. A necessary and sufficient condition for the control law (40) to asymptotically zero δr_{ref} is that $|1 - k_{ref}| < 1$. If $k_{ref} = 1$, $\delta r_{ref} = 0$ is achieved in the finite time

$$N_{ref} + 1 = \text{floor}\left(\frac{|\delta r_{0,ref}|}{2bu_{x,\max}} \right) + 1 . \tag{41}$$

Proof. The necessary and sufficient condition makes the radial dynamics, i.e. the first row of (39), asymptotically stable. Assuming a deadbeat control, namely $k_{ref} = 1$, equation (41) is equivalent to write

$$0 \le \frac{\left|\delta r_{ref}\left(N_{ref}\right)\right|}{2bu_{x,\max}} = \frac{\left|\delta r_{0,ref}\right|}{2bu_{x,\max}} - N_{ref} < 1. \tag{42}$$

Thus $2bu_{ref}\left(N_{ref}\right) = -\delta r_{ref}\left(N_{ref}\right)$ and $\delta r_{ref}\left(N_{ref}+1\right) = 0$. □

To give a numerical value, assume $u_{x,\max} \cong \omega_{nom}^2 \approx 1$ μm/s^2 which corresponds to about 1 mN thrust for a 1000 kg satellite, which is an upper bound to NGGM mass. Then the number of orbits to achieve the nominal altitude is

$$N_{ref} \cong \frac{\left|\delta r_{0,ref}\right|}{4\pi} \cong 80 \ (\approx 5 \text{ days}) \ @ \left|\delta r_{0,ref}\right| \cong 1 \text{ km}. \tag{43}$$

For a drag-free satellite, the above figure applies both to ascending and descending altitude.

The second equation in (39) allows computing the effect of $u_{x,ref}$ on the orbit angular rate, which is hidden in the total speed δs_{ref}. Differentiating the last equation in (14), the angular rate perturbation $\delta\omega_{y,ref}$ becomes related to the radial perturbation as follows

$$\delta\omega_{y,ref}\left(n\right) = -\frac{3}{2}\frac{\omega_{nom}}{r_{nom}}\delta r_{ref}\left(n\right). \tag{44}$$

State predictor

The embedded model (24) is driven by commands to be computed by control law and noise components. Noise estimator is in charge of real-time estimating such components, and therefore of updating disturbance and controllable state variables of the embedded model. The ensemble that consists of embedded model and noise estimator behaves like a state predictor, but their aim is wider since they aim to keep updated the disturbance state x_{dx} to be cancelled by the control law. Noise is estimated by closing the feedback around the embedded model, the feedback being driven by the model error e_r. Since only the state variables δr and x_{dx} are observable from the output y_r in (24), the embedded model simplifies to

$$\begin{aligned}
\begin{bmatrix}\delta r\\ x_{dx}\end{bmatrix}\left(n+1\right) &= \begin{bmatrix}1 & 1\\ 0 & 1\end{bmatrix}\begin{bmatrix}\delta r\\ x_{dx}\end{bmatrix}\left(n\right) + \begin{bmatrix}2b\\ 0\end{bmatrix}u_x\left(n\right) + \begin{bmatrix}w_x\\ w_{dx}\end{bmatrix}\left(n\right)\\
y_r\left(n\right) &= \begin{bmatrix}1 & 0\end{bmatrix}\begin{bmatrix}\delta r\\ x_{dx}\end{bmatrix}\left(n\right) + e_r\left(n\right) = y_{mr}\left(n\right) + e_r\left(n\right)
\end{aligned} \tag{45}$$

The noise estimator is the static feedback

$$\begin{bmatrix}w_r\\ w_{dx}\end{bmatrix}\left(n\right) = \begin{bmatrix}l_x\\ l_{dx}\end{bmatrix}e_r\left(n\right). \tag{46}$$

In the Kalman filter framework, the gains l_x and l_{dx} are designed to minimize the prediction error covariance. Here, they are designed to guarantee stability of the whole closed-loop system in the presence of neglected dynamics like that due to notch filter. In fact, because of notch filter, GNSI measurement errors become negligible with respect to the altitude tolerance in Table 1, and Kalman optimization becomes unnecessary. To guarantee stability, an approximation of the neglected dynamics must be known. Then the state equation (or the transfer function ∂P_r in the linear case) of the 'fractional error dynamics' from the model output y_{mr} to the model error e_r must be built. The Z-transform input-output relation is the following

$$e_r\left(z\right) = \partial P_r\left(z\right) y_{mr}\left(z\right). \tag{47}$$

A sufficient stability condition [28] corresponds to

$$\max_{|f|<f_{\max}} \left|V_r\left(e^{j2\pi fP_{nom}}\right)\partial P_r\left(e^{j2\pi fP_{nom}}\right)\right| \le \eta_r < 1, \tag{48}$$

where V_r is the overall control transfer function, which under the assumptions as in [28] can be approximated by the complementary sensitivity of the state predictor

$$V_r(z) \cong V_{pr}(z) = \frac{y_{mr}(z)}{y_r(z)}. \tag{49}$$

The stability margin is η_r^{-1}. The product $V_r \partial P_r$ can be referred as the closed-loop error dynamics. Figure 8 shows the Nyquist plot of the open-loop and closed-loop fractional error dynamics. The open-loop tends to include the critical point $-1 + j0$, whereas the closed loop is inside the unit circle, thus guaranteeing stability with a margin larger than one octave, $\eta_r^{-1} > 2$. The margin is strictly related to the values of the noise estimator gains in (46) and to the BW of V_r, which has been designed close to 0.02 mHz, i.e. one tenth of $\tilde{f}_m$.

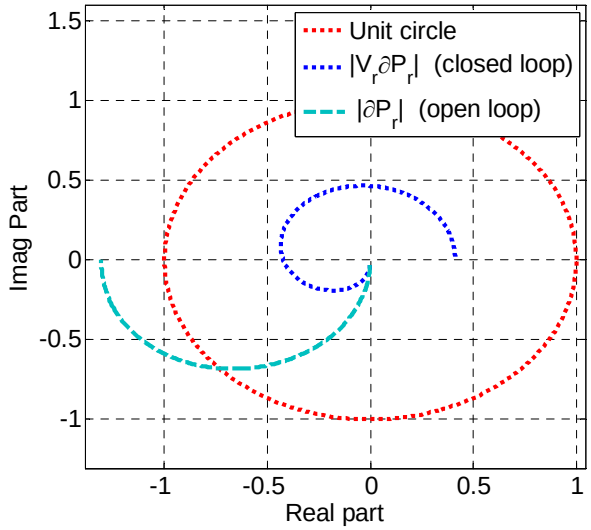

Figure 8 Nyquist plot of the open-loop and closed-loop fractional error dynamics.

The altitude control

It has been shown in [28] that the stability condition (48) allows the control law to be designed model-based, thus forgetting model errors. However, the closed-loop performance, that is to say the statistics of the tracking error, depends on the overall control transfer function V_r in (49), which in turn is dominated by the state predictor complement V_{pr}. Since we are just interested to asymptotic performance, we forget the state predictor dynamics (which is otherwise essential for guaranteeing stability), that is to say we assume $V_{pr} \cong 1$. In other terms, we restrict to a frequency domain which is upper limited by the state predictor BW.

Under such assumptions, that may be referred to as 'ideal' or 'model-based', the altitude control must asymptotically stabilize the radial dynamics, 'exactly' cancel the disturbance d_x and track the reference perturbation δr_{ref} given by (39). To this end, the 'ideal' control law writes as

$$\begin{aligned} 2bu_x(n) &= 2bu_{x,ref}(n) + k_r\left(\delta r_{ref} - \delta r\right)(n) - 2bx_{dx}(n) \\ u_z(n) &= 0 \\ \delta r_{err}(n) &= \delta r_{ref}(n) - \delta r(n) \end{aligned}, \tag{50}$$

where δr_{err} is the radial tracking error. The control law cannot include the noise w_x in (24) as the latter is unpredictable. It is immediate to compute the error equation as a difference between (39) and (24) under the control law (50). Adopting similar notations as in (50) one finds

$$\begin{bmatrix}\delta r_{err}\\ \delta s_{err}\\ \delta x_{err}\end{bmatrix}(n+1)=\begin{bmatrix}1-k_r & 0 & 0\\ -k_r & 1 & 0\\ 3k_r & -6\pi & 1\end{bmatrix}\begin{bmatrix}\delta r_{err}\\ \delta s_{err}\\ \delta x_{err}\end{bmatrix}(n)+b\begin{bmatrix}-2 & 0\\ -1 & 0\\ 3 & 2\end{bmatrix}\begin{bmatrix}w_x\\ d_z=x_{dz}+w_z\end{bmatrix}(n). \tag{51}$$

By assuming $|1-k_r|<1$, the radial error converges to zero in the mean, but fluctuates because of the residual w_x. Secular components only affect the speed δs and the longitudinal perturbation δx, and are forced by w_x and by the mean value d_{z0} of d_z. A typical value of the GOCE-class accelerometers is $|d_{z0}|<\omega_{nom}^2\approx 1\ \mu\text{m/s}^2$. The following Theorem provides the statistics of the error components in (51).

Theorem 4. Assuming that the stability condition $|1-k_r|<1$ holds and that the bounded noise w_x has the statistics of (25), the asymptotic mean value and standard deviation of the tracking errors in (51) are:

$$\begin{aligned}&\mathcal{E}\{\delta r_{err}(n)\}\to 0,\ \sigma\{\delta r_{err}(n)\}\to b\frac{\sigma_{wx}}{k_r}\cong\frac{0.02\pi}{k_r}\\ &\mathcal{E}\{\delta s_{err}(n)\}\to 0,\ \sigma\{\delta s_{err}(n)\}\to bS_{wx}\sqrt{n/P_{nom}}\cong 0.06\sqrt{n/P_{nom}}\\ &\left|\mathcal{E}\{\delta x_{err}(n)\}\right|\to 2b|d_{z0}|n\cong 4\pi n,\ \sigma\{\delta x_{err}(n)\}\to 6bS_{wx}n\sqrt{n/(3P_{nom})}\cong 0.1n\sqrt{n/P_{nom}}\end{aligned}\quad\square \tag{52}$$

The last row of (52) shows that the longitudinal perturbation error δx_{err} is diverging as expected being not controlled, whereas the longitudinal rate error δs_{err} is statistically bounded. It is of interest to estimate the maximum longitudinal error at the end of the mission life. A 10-year mission which is the NGGM target corresponds to about $N_{\max}\cong 57000$ orbits, and the maximum error is found to be

$$|\delta x_{err}(N_{\max})|\approx 720\pm 20(1\sigma)\ \text{km}\ (<1\text{deg}), \tag{53}$$

which is a negligible value.

Formation control

The formation control is organized like the altitude control, and consists of three subsystems, reference generator, noise estimator and control law built around the embedded model. As already said, formation control implements both distance and altitude control.

Reference generator

The reference generator has the aim of smoothing the distance and radial trajectories when the actual mean distance and altitude are not close to the reference values d_{nom} and r_{nom}. In practice, the reference generator mechanizes formation and orbit acquisition, with the constraints of the millinewton thruster authority.

The reference embedded model is equation (30), but free of disturbance and noise. Using the command $\mathbf{v}$ as in (27), it can be written as

$$\begin{aligned}&\mathbf{x}_{ref}(n+1)=A_c\mathbf{x}_{ref}(n)+B_c\mathbf{v}_{ref}(n),\ \mathbf{x}_{ref}(0)=\mathbf{x}_{ref,0}\\ &\mathbf{x}_{ref}=\begin{bmatrix}\delta d_{ref}\\ \delta\rho_{x,ref}\\ \delta r_{z,ref}\end{bmatrix}\end{aligned}. \tag{54}$$

Assuming the components of $\mathbf{u}$ in (29) are bounded by $u_{\max}\cong\omega_{nom}^2$, the bounds to the components of $\mathbf{v}_{ref}$ in (54) derive from (29), and by neglecting $\alpha<<1$, hold

$$b\mathbf{v}_{\max} = b\begin{bmatrix} v_{1,\max} \\ v_{2,\max} \\ v_{3,\max} \end{bmatrix} \cong 2\pi \begin{bmatrix} 2 \\ 2 \\ 1 \end{bmatrix} \ [m]. \tag{55}$$

To be conservative assume simultaneous orbit and formation acquisition, and assume a constant reference command as for the altitude control. In practice we want to zero the initial perturbation $\mathbf{x}_{ref,0}$ during a period of N orbits, while respecting the bounds in (55). Solving the free and forced response of (54), one finds the following solution for a constant command $\mathbf{v}_{ref}$:

$$b\mathbf{v}_{ref} = -\frac{1}{2N}\begin{bmatrix} 0 & 1 & 0 \\ 1 & \dfrac{3\pi N}{2} & 0 \\ 0 & 0 & 1 \end{bmatrix} \mathbf{x}_{ref,0}. \tag{56}$$

The least acquisition period N is obtained by forcing (56) to agree with (55), which rule provides the three lower bounds $N_{j,\min}$, $j = 1,2,3$, as follows

$$\begin{bmatrix} N_{1,\min} \\ N_{2,\min} \\ N_{3,\min} \end{bmatrix} = \frac{1}{8\pi}\begin{bmatrix} \left|\delta\rho_{x,ref}(0)\right| \\ \left|\delta d_{ref}(0)\right| + 3\pi N\left|\delta\rho_{x,ref}(0)\right| \\ 2\left|\delta r_{z,ref}(0)\right| \end{bmatrix} \geq \frac{1}{8\pi}\begin{bmatrix} \left|\delta\rho_{x,ref}(0)\right| \\ \left|\delta d_{ref}(0)\right| + \dfrac{3}{8}\left|\delta\rho_{x,ref}(0)\right|^2 \\ 2\left|\delta r_{z,ref}(0)\right| \end{bmatrix}. \tag{57}$$

Equation (56) points out some difficulty in performing simultaneous orbit and formation acquisition, because of the limited command authority. The critical term is the second row in (57), which shows that the 'radial difference' is affected by the distance perturbation until the zero state is achieved. Depending on $\left|\delta\rho_{x,ref}(0)\right|$, no room may exist for $v_{2,ref}$ to zero $\left|\delta d_{ref}(0)\right|$ until $\left|\delta\rho_{x,ref}(0)\right| = 0$. This is consistent with the strategy of an earlier altitude control for preparing formation acquisition and control. Equation (57) shows that initial distance and radius errors of the order of 1 km can be zeroed in a few days. A (mean) radial difference of 100 m demands a formation acquisition lasting about 10 days. Of course, these values are such to be scaled down by a broader command authority.

State predictor and formation control

By disposing of one measurement for each DoF in (27), the state predictor can be split into three separate predictors of the same type as in (45) and (46). The gain design is the same as for the altitude control. No further details are given. Given the reference trajectory and commands from (54) and the state variables from the state predictor, the formation control law is a multivariate version of the altitude law in (50). The 'ideal' control law holds

$$\begin{aligned} \mathbf{u}(n) &= S^{\dagger}\mathbf{v}(n) \\ \mathbf{v}(n) &= \mathbf{v}_{ref}(n) + B_c^{-1}\left(K\left(\mathbf{x}_{ref} - \mathbf{x}_c\right)(n) - \mathbf{x}_d(n)\right). \\ \mathbf{x}_{err} &= \mathbf{x}_{ref} - \mathbf{x}_c \end{aligned} \tag{58}$$

The properties of (30) and (58) are established by the following Theorem.

Theorem 5. The tracking error $\mathbf{x}_{err}$ in (58) is bounded and the mean value converges to zero if and only if $A_c - K$ is asymptotically stable.

Proof. The proof follows from the error equation

$$\mathbf{x}_{err}(n+1) = (A_c - K)\mathbf{x}_{err}(n) - \mathbf{w}(n),\ \mathbf{x}_{err}(0) = \mathbf{x}_{err,0}. \tag{59}$$

The gain matrix K can be designed to decouple the response of (59), which, given the closed-loop eigenvalues $\Lambda_c = \{1-\gamma_1, 1-\gamma_2, 1-\gamma_3\}$ provides

$$K = \begin{bmatrix} \gamma_1 & -3\pi & 0 \\ 0 & \gamma_2 & 0 \\ 0 & 0 & \gamma_3 \end{bmatrix}. \tag{60}$$

Drag-free control

According to Theorem 1, to requirement (35) and to equation (33), the drag-free command of the satellite $k = 1,2$ and of the FLOF axis $j = x, y, z$, is given by

$$\begin{aligned} u_a(i) &= -x_d(i) + a_{ref}\left(n(i)\right) \\ a_{ref}\left(n(i)\right) &= u_{jk}\left(n(i)\right) \end{aligned}, \tag{61}$$

where $n(i)$ has been defined in (23) and u_{jk} in (29). The noise component $w_d(i)$ cannot be rejected being simultaneous to $u_a(i)$. The next theorem states how to measure x_d through the embedded model (33).

Theorem 6. The only way to measure x_d in real-time is to correlate $\mathbf{w}_d$ in (33) to the model error $e_a = y_a - x_a$. Restricting to a linear and time invariant (LTI) correlation, a necessary and sufficient condition, under bounded e_a, for guaranteeing a bounded measurement error is the static correlation

$$\mathbf{w}_d(i) = L_d e_a(i), \tag{62}$$

where L_d is a 3×1 constant vector such that $A_d - L_d C_d$ is asymptotically stable.

Proof. The proof follows from Lemma 7 and from L_d being the gain vector of a LTI state observer. □

The three gains of L_d are obtained from the state-predictor eigenvalues $\Lambda_d = \{1-\gamma_{d1}, 1-\gamma_{d2}, 1-\gamma_{d3}\}$. A main assumption in Theorem 6 is that e_a is bounded, which is straightforward if e_a is command-independent. Actually it encodes the effects of the thruster-to-accelerometer neglected dynamics (anti-aliasing filter, thruster response time) not fully accounted for by β_d. Which negligence demands restriction of the state observer bandwidth to below 0.5 Hz (one tenth of the Nyquist frequency of 5 Hz, as for GOCE satellite [14], [26]).

Only a brief account of the eigenvalue design is given now, since it has been partly reported in [14] and [26]. Because requirements in Figure 2 and Table 1 are given in the frequency domain, the latter is appealing also for control design. According to EMC methodology, the key design equation is obtained by combining (33), (61) and (62) into the residual non-gravitational acceleration as follows

$$\begin{aligned} a(z) &= S_d(z, \Lambda_a) d_a(z) - V_d(z,, \Lambda_a)\left(b_a + M_d^{-1}(z) e_a\right)(z) \\ M_d(z) &= (z - 1 + \beta_d)^{-1} \\ S_d(z) &= 1 - V_d(z) \end{aligned}, \tag{63}$$

where S_d is the overall drag-free control sensitivity and V_d the complementary sensitivity as in (48). They depend on the eigenvalue set Λ_a. The time signals of the Z-transforms d_a and b_a in (63) have been defined in (33), and correspond to the non-gravitational acceleration and to the accelerometer bias/drift, respectively. Equation (63) formulates the well-known result that sensitivity, being high-pass, cancels the low-frequency components of d_a as requested, whereas the low-frequency error b_a passes into a, V_d being low-pass. However the main role of V_a, as pointed out by (48) is to guarantee closed-loop stability in the presence of a neglected dynamics $\partial P_a(z)$ affecting the model error e_a. Combination of stability and performance requirements leads to a pair of inequalities in the frequency domain from DC to $f_{\max} = 5$ Hz

$$\begin{aligned} &\left|V_d\left(f,\Lambda_d\right)\partial P_a\left(f\right)\right| \le \eta_a < 1 \\ &\frac{1}{\left(1-\eta_a\right)^2}\left(\left|S_d\left(f,\Lambda_d\right)\right|^2 S_{da}^2\left(f\right)+\left|V_d\left(f,\Lambda_d\right)\right|^2 S_{ba}^2\left(f\right)\right) \le S_{a,\max}^2\left(f\right), \end{aligned} \tag{64}$$

where $S_{a,\max}$ is the PSD bound in Figure 2, S_{da} and S_{ba} are bounds of the experimental spectral densities of d_a and b_a respectively. Neglecting S_{ba} in the second inequality of (64), both inequalities can be combined in a functional to be maximized in the frequency domain and minimized with respect to Λ_d:

$$\begin{aligned} &\Lambda_d^* = \arg\min_{\Lambda_d} J\left(\Lambda_d,\eta\right) \le 1 \\ &J\left(\Lambda_d,\eta\right) = \max_{|f|\le f_{\max}} \alpha W_{\partial P}\left(\cdot\right)\left|V_d\left(f,\Lambda_d\right)\right| + \left(1-\alpha\right) W_{da}\left(\cdot\right)\left|S_d\left(f,\Lambda_d\right)\right| \end{aligned}. \tag{65}$$

The weights $W_{\partial P}$ and W_{da} derive from (64) and depend on f and η. The control problem would result unfeasible if $\min_{\Lambda_d} J\left(\Lambda_d,\eta\right) \ge 1$. By expressing the eigenvalues $\lambda_{dk} = 1-\gamma_{dk}$, $k = 1,2,3$ in terms of a single complementary eigenvalue γ_d, and by fixing $\eta = \alpha = 0.5$, the plot in Figure 9 has been obtained. The control problem results to be feasible and leaves some margin. The optimal $\gamma_d^* \cong 0.25$ corresponds to a BW of 0.4 Hz, as expected.

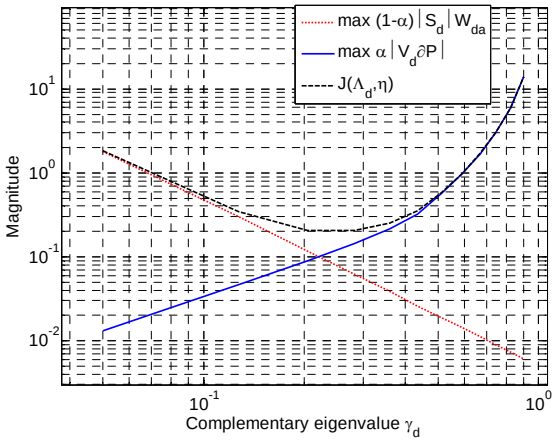

Figure 9 The functional J in (65) versus a single complementary eigenvalue.

SIMULATED RESULTS

Figure 10 to Figure 14 show simulated results from a complete orbit and attitude simulator, that includes the science-phase AOCS. Thruster noise and aerodynamics have been simplified. The mean orbit altitude is 340 km and the pendulum formation has been simulated. Figure 10 shows the formation command components. The lateral command (FLOF y-axis) is zero because formation angular control is inactive. Because of the strict attitude, body frame and FLOF components coincide. Variables are in millinewton. Time is in ks (kiloseconds), and 2800 ks correspond to about one month. The longitudinal command tends to be constant, whereas the radial command slowly fluctuates. The difference is due to a larger drift of the radial accelerometer axis.

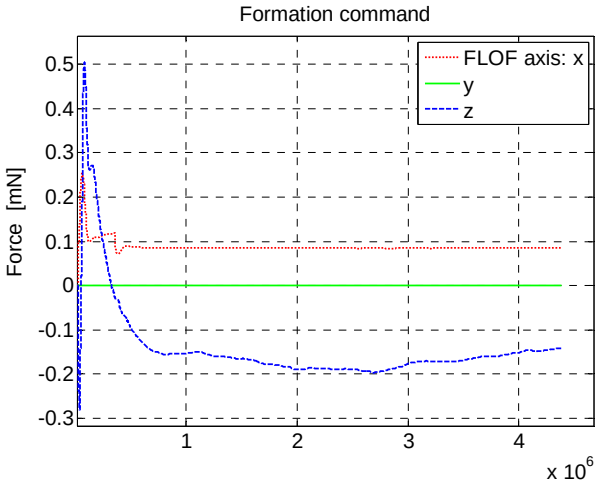

Figure 10 Formation commands in force units.

Figure 11 shows altitude and distance tracking errors. The altitude is the mean formation altitude corresponding to the radius r_z. The strip and slow drift of the altitude tracking error are due to inaccurate orbit average and sampling ($<0.0005P_{nom}$) because of time quantization. It is such to generate a beat component. The abscissa is reported as the orbit count. The distance transient (partially visible) is due to a formation acquisition from an initial error of 800 m.

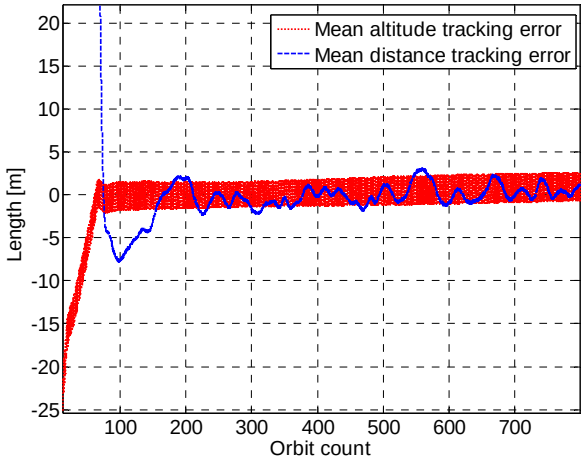

Figure 11 Formation altitude and distance tracking errors.

Figure 12 shows the time profile of the residual non-gravitational acceleration as a result of drag-free and formation control.

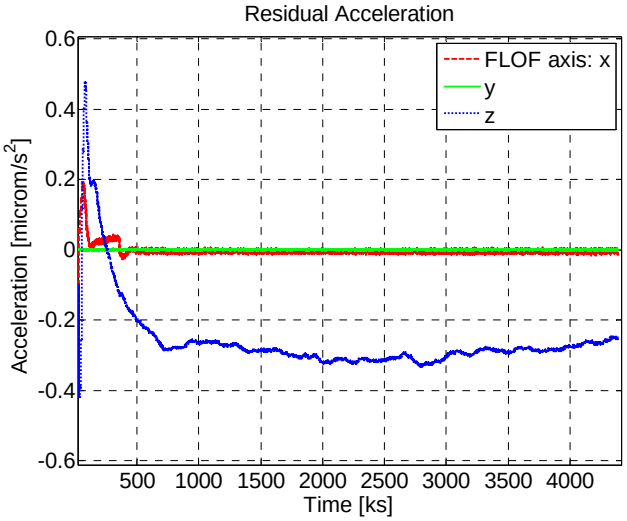

Figure 12 Residual CoM acceleration.

The different residuals of the longitudinal and radial FLOF axes follows from the matrix (29) and the control law (58). Let us denote the drag-free residual vector $\mathbf{d} = -S\mathbf{b}_a$ to be rejected by the formation control as

$$\mathbf{b}_a = \begin{bmatrix} b_{1x} \\ b_{1z} \\ b_{2x} \\ b_{2z} \end{bmatrix}. \tag{66}$$

The generic component corresponds to the sum $d_a - x_d = -b_a + (w_d = 0)$ in (33), where $-x_d$ is the drag-free command in (61), b_a is the accelerometer bias/drift and the noise component is assumed to be zero. The residual acceleration of the formation and drag-free control u_a in (61) holds

$$\mathbf{a} = \mathbf{u} - \mathbf{b}_a. \tag{67}$$

Now assuming zero reference and zero tracking error in (58), we have for $\alpha = 0$

$$\mathbf{a} = \left(S^{\dagger}S - I\right)\mathbf{b}_a \cong \begin{bmatrix} 0 \\ (b_{1z} + b_{2z})/2 \\ 0 \\ (b_{1z} + b_{2z})/2 \end{bmatrix}. \tag{68}$$

Figure 12 fits equation (68). Indeed the longitudinal residual (FLOF x-axis) is zero-mean, whereas the formation command in Figure 10 tends to a nonzero term (the accelerometer bias to be rejected). Instead the radial residual (FLOF z-axis) is not zero mean, as the second and fourth rows in (68) predict.

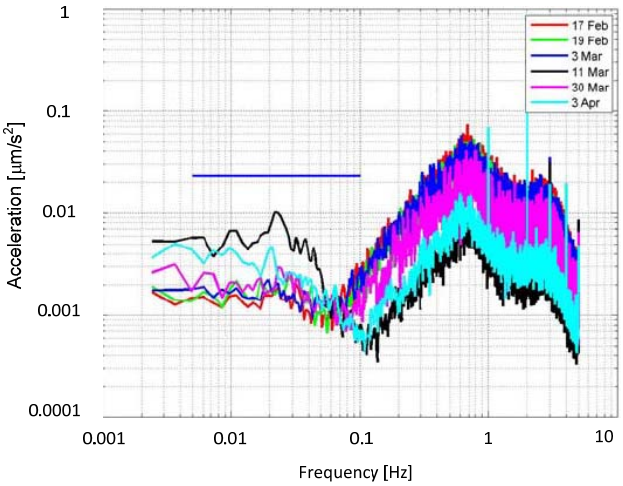

Figure 13 Experimental spectral density of the longitudinal residual acceleration (GOCE satellite).

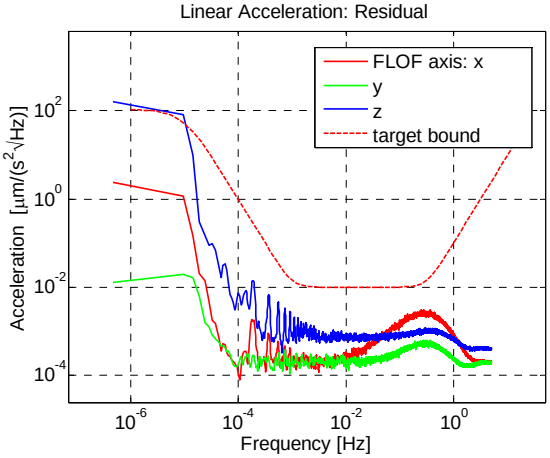

Figure 14 Simulated spectral density of the non-gravitational residuals for a single satellite.

For comparison, Figure 13 shows the experimental drag-free residuals of the GOCE satellite along the axis aligned with the velocity vector (the unique GOCE drag-free axis). The horizontal segment above the spectral profiles indicates the upper limit equal to 0.025 $\mu m/s^2/\sqrt{Hz}$ in the range $\mathscr{B}$ of (38). Residuals vary with the epoch because the thermosphere density is highly sensible to solar activity. The frequency of the profile peak, close to 0.5 Hz, is the drag-free BW, close to the optimal value of Figure 9. Figure 14 shows the PSD of the time profiles in Figure 12. The PSD pertains to leader satellite of a pendulum formation. The high-frequency shape looks smaller than Figure 13, because drag model and thruster noise were to some extent simplified in the simulated model. Formation control is such not to overshoot the spectral density. The formation control contribution is the series of decreasing resonances starting at the orbit frequency of 0.2 mHz. The peaks decrease at a rate of -20dB/decade, which is typical of a stepwise profile.

CONCLUSION

The paper outlines the mandatory design in terms of disturbance dynamics, their measurement and rejection for the formation and drag-free control of a two-satellite long-distance formation flying at low Earth orbit. A hierarchical control design has been designed, taking advantage of wide-

band acceleration measurements capable of cancelling non gravitational accelerations. Then narrower outer loops can be designed for keeping constant orbit altitude and formation distance. Altitude control has been firstly solved stand alone, based on new dynamic equation of the satellite radius perturbations. Since altitude requirements only concern secular components less than the orbit frequency, the embedded model of the altitude has been obtained by discretizing the continuous time equations at the orbit frequency. This allows designing a stepwise altitude control, which is sufficiently smooth not to degrade the drag-free residuals. The same method has been adopted for designing a formation control, which is capable of controlling in an integrated manner distance and altitude. Simulated and experimental results are provided.

ACKNOWLEDGMENTS

Part of the work of Enrico Canuto, Politecnico di Torino, has been done under a sub-contract with the European Space Agency (ESA), Thales Alenia Space Italia (TASI), Turin, Italy, being the prime contractor. Luigi Colangelo, Politecnico di Torino, is a Ph.D. student of Politecnico di Torino under the ESA's Networking/Partnering Initiative (NPI), with the financial support of ESA and TASI. The work Authors acknowledge reviewers' remarks and suggestions.

APPENDIX

Consider the first-order state equation

$$\begin{aligned} &\dot{x}(t) = sh(x,t) + bu(t),\ x(0) = x_0 \\ &y(t) = x(t) \\ &s = \pm 1 \end{aligned} \tag{68}$$

where the only assumption on $h(\cdot)$ is that is sector bounded as follows

$$\begin{aligned} &0 \le \frac{h(x,t)}{x(t)} \le p,\ x(t) \ne 0 \\ &0 < p < p_{\max} < \infty \end{aligned}, \tag{68}$$

and that $p_{\max}$ is known. The control goal is to asymptotically zero initial condition. No specific response time is imposed. The control law

$$bu_0(t) = -(p_{\max} + \varepsilon) y(t),\ \varepsilon > 0 \tag{68}$$

stabilizes (68) also in the worst case of $h(x,t) = p_{\max} x(t)$. The worst-case condition provides a bound to closed-loop state and command response as follows

$$\begin{aligned} &|x| \le |x_0| e^{-\varepsilon t} \\ &b|u_0| \le (p_{\max} + \varepsilon)|x_0| e^{-\varepsilon t} \end{aligned}. \tag{68}$$

Consider now a control law typical of the Embedded Model Control:

$$bu_1(t) = -\varepsilon y(t) - sh(x,t),\ \varepsilon > 0, \tag{68}$$

which explicitly compensates for h without any a priori knowledge. The bound (68) only serves for tuning the estimator of h and for fixing a bound on the estimation error variance, which is here neglected. State and command are now bounded by

$$\begin{aligned} &|x| \le |x_0| e^{-\varepsilon t} \\ &b|u_1| \le \varepsilon |x_0| e^{-\varepsilon t} + |h(x,t)| \le (p + \varepsilon)|x_0| e^{-\varepsilon t} \end{aligned}. \tag{68}$$

The command ratio

$$\frac{|u_1|}{|u_0|} = \frac{p+\varepsilon}{p_{\max}+\varepsilon} < 1 \tag{68}$$

is always in favor of u_1 since it tends to unit only for $\varepsilon \to \infty$.

REFERENCES

[1] S. Cesare, S. Mottini, F. Musso, M. Parisch, G. Sechi, E. Canuto, M. Aguirre, B. Leone, L. Massotti and P. Silvestrin, "Satellite formation for a next generation gravimetry mission", in R. Sandau et al. eds., *Small satellite missions for Earth observations*, Springer, Heidelberg, pp. 125-134, 2010.

[2] M. Fehringer, G. André, D. Lamarre and D. Maeusli, "GOCE and its gravity measurement system", *ESA Bulletin*, Vol. 133, February 2008, p. 15-23.

[3] E. Canuto, P. Martella and G. Sechi, "Attitude and drag control: an application to the GOCE satellite", *Space Science Reviews*, Vol. 108, 2003, pp. 357-366.

[4] B.D. Tapley, S. Bettadpur, M. Watkins and C. Reigber, "The gravity recovery and climate experiment: Mission overview and early results", *Geophys. Res. Lett.,* Vol. 31, No. 9, May 2004.

[5] K. Danzmann, "The Status of LISA", *38th COSPAR Scientific Assembly*, 18-15 July 2010, Bremen, Germany, pp. 2.

[6] P. Touboul, G. Metris, A. Robert, A. Levy and G. Campergue, "The MICROSCOPE mission: a challenging free fall test", *38th COSPAR Scientific Assembly*,18-15 July 2010, Bremen, Germany, pp. 6.

[7] W. Fichter, P. Gath and S. Vitale, "LISA Pathfinder drag-free control and system implications", *Classical and Quantum Gravity,* Vol.22, 2005, pp. 139-148.

[8] W.J. Bencze, D.B. DeBra , L. Herman , T. Holmes, M. Adams , G.M. Keiser and C.W.F. Everitt, "On-orbit performance of the Gravity Probe B drag-free translation control system", *Advances in Space Research*, Vol. 40, No. 1, 2007, pp.1-10.

[9] E. Canuto and L. Colangelo "Angular drag-free control and fine satellite-to-satellite pointing for the Next Generation Gravity Missions", in *Proc. of the 13th European Control Conference (ECC 2014),* Strasbourg, France, 24-27 June 2104, pp. 3017-3022.

[10] B. Lange, "The drag-free satellite*", AIAA Journal*, Vol. 2. No.9, September 1964, pp.1590-1606.

[11] D. B. DeBra, "Drag-free control for fundamental physics missions", *Advances in Space Research*, Vol. 32, No. 7, October 2003, pp. 1221-1226.

[12] Staff of the Space Department of the Johns-Hopkins-University Applied Physics Laboratory and Staff of the Guidance and Control Laboratory at Stanford University, "A Satellite Freed of All but Gravitational Forces: TRIAD I*", AIAA J. Spacecraft*, Vol. 11, No. 9, September 1974, pp.637-644.

[13] E. Canuto, A, Molano-Jimenez, C. Perez-Montenegro and L. Massotti, *"*Long-distance drag-free, low-thrust, LEO formation control for Earth gravity monitoring", *Acta Astronautica,* vol. 69, 2011, pp. 571-582.

[14] E. Canuto *"*Drag-free and attitude control for the GOCE satellite", *Automatica*, Vol. 44, No. 7, 2008, pp. 1766-1780.

[15] E. Canuto "Embedded Model Control: outline of the theory", *ISA Transactions*, Vol. 46, No. 3, 2007, pp. 363-377.

[16] E. Canuto, W. Acuna-Bravo, A. Molano-Jimenez and C. Perez-Montenegro, "Embedded Model Control calls for disturbance modelling and rejection", *ISA Transactions*, Vol. 51, No. 5, 2012, pp. 584-595.

[17] L. Pettazzi, A. Lanzon, S. Theil and A. Ercoli Finzi, "Design of robust drag-free controllers with given structure", *Journal of Control, Guidance and Dynamics,* Vol. 32, No. 5, 2009, pp. 1609-1621.

[18] W. Fichter, A. Schleicher, L. Szerdahelyi, S. Theil and P. Airey, "Drag-free control system for frame dragging measurements based on cold atom interferometry", *Acta Astronautica*, Vol. 57, No. 10, Nov. 2005, pp. 788-799.

[19] S-F. Wu and D. Fertin, "Spacecraft drag-free attitude control system design with quantitative feedback theory", *Acta Astronautica*, Vol. 62, No. 12, June 2008, pp. 668-682.

[20] W. H. Clohessy and R.S. Wiltshire "Terminal guidance systems for satellite rendezvous", *Journal of the Aerospace Sciences*, Vol. 27, No. 9, September 1960, pp. 653-658.

[21] G. Hill "Researches in the lunar theory", *American Journal of Mathematics*, Vol. 1, 1878, pp. 5-26.

[22] S. R. Ploen, D. P. Scharf, F. Y. Hadaegh and A. B. Acikmese, "Dynamics of Earth orbiting formations", *AIAA Guidance, Navigation and Control Conf. and Exhibit,* 16-19 August, 2004, Providence, Rhode Island, Paper AIAA 2004-5134.

[23] V. M. Guibout and D. J. Scheeres "Spacecraft formation dynamics and design", *J. Guidance, Control and Dynamics,* Vol. 29, No. 1, January-February 2006, pp. 121-133.

[24] G. Inalhan, M. Tillerson and J. P. How, "Relative dynamics and control of spacecraft formations in eccentric orbits", *J. Guidance, Control and Dynamics,* Vol. 25, No. 1, January-February 2002, pp. 48-59.

[25] H. Schaub "Spacecraft relative orbit geometry description through orbit element differences*", 14th US National Congress of Theoretical and Applied Mechanics*, Blacksburg, VA, June 23-28, 2002.

[26] E. Canuto, A. Molano and L. Massotti, "Drag-free control of the GOCE satellite: noise and observer design", *IEEE Trans. Control Systems Technology*, Vol. 18, No.2, March 2010, pp. 501-509.

[27] C. Steiger, A. Da Costa, P.P. Emanuelli, R. Floberhagen and M. Fehringer, "Evolution of flight operations for ESA's gravity mission GOCE", Proc. of the *12th International Conference on Space Operations*, Stockholm, Sweden, June 11-15, 2012.

[28] E. Canuto, W. Acuna-Bravo and C. Perez-Montenegro, "Robust control stability using the error loop", *Int. Journal of Mechatronics and Automation*, Vol. 3, No. 2, 2013, pp. 94-109.

[29] J.M. Sidi, *Spacecraft dynamics and control. A practical engineering approach*. Cambridge University Press, 1997.